THE ASTRONOMICAL JOURNAL, 115:168–192, 1998 January

EARLY EVOLUTION OF THE GALACTIC HALO REVEALED FROM *HIPPARCOS* OBSERVATIONS OF METAL-POOR STARS

MASASHI CHIBA
National Astronomical Observatory, Mitaka-shi, Tokyo 181, Japan
AND
YUZURU YOSHII[1]
Institute of Astronomy, Faculty of Science, University of Tokyo, Mitaka-shi, Tokyo 181, Japan
Received 1997 July 21; revised 1997 September 22

ABSTRACT

The kinematics of 122 red giant and 124 RR Lyrae stars in the solar neighborhood are studied using accurate measurements of their proper motions obtained by the *Hipparcos* astrometry satellite, combined with their published photometric distances, metal abundances, and radial velocities. A majority of these sample stars have metal abundances of [Fe/H] ≤ -1 and thus represent the old stellar populations in the Galaxy. The halo component, with [Fe/H] ≤ -1.6, is characterized by a lack of systemic rotation [$(\langle U\rangle, \langle V\rangle, \langle W\rangle) = (16 \pm 18, -217 \pm 21, -10 \pm 12)$ km s^{-1}] and a radially elongated velocity ellipsoid [$(\sigma_U, \sigma_V, \sigma_W) = (161 \pm 10, 115 \pm 7, 108 \pm 7)$ km s^{-1}]. About 16% of such metal-poor stars have low orbital eccentricities ($e < 0.4$), and we see no evidence of a correlation between [Fe/H] and e. Based on the model for the e-distribution of orbits, we show that this fraction of low-e stars for [Fe/H] ≤ -1.6 is explained by the halo component alone, without introducing the extra disk component claimed by recent workers. This is also supported by the absence of a significant change in the e-distribution with height from the Galactic plane. In the intermediate-metallicity range ($-1.6 <$ [Fe/H] ≤ -1), we find that stars with disklike kinematics have only modest effects on the distributions of rotational velocities and e for the sample at $|z| < 1$ kpc. This disk component appears to constitute only $\sim 10\%$ for $-1.6 <$ [Fe/H] ≤ -1 and $\sim 20\%$ for $-1.4 <$ [Fe/H] ≤ -1. It is also verified that this metal-weak disk has a mean rotation of ~ 195 km s^{-1} and a vertical extent of ~ 1 kpc, which is consistent with the thick disk's dominating at [Fe/H] $= -0.6$ to -1. We find no metallicity gradient in the halo, whereas there is an indication of a metallicity gradient in the metal-weak tail of the thick disk. The implications of these results for the early evolution of the Galaxy are also presented.

Key words: Galaxy: abundances — Galaxy: evolution — Galaxy: halo

1. INTRODUCTION

Our understanding of how disk galaxies like our own were formed has advanced greatly in recent years. Modern large telescopes armed with sensitive detectors are about to reach the epochs of galaxy formation. Ultrafaint imaging in the deep universe has revealed a number of blue, irregularly shaped disks, occasionally accompanied by fuzzy blobs (Williams et al. 1996). Follow-up spectroscopic studies have confirmed that these disklike systems are indeed rotationally supported (e.g., Vogt et al. 1996). Another line of evidence for disk galaxy formation has emerged from the studies of quasar absorption-line systems (Pettini et al. 1995; Lu et al. 1996). These absorbers associate heavy elements with abundances much less than the solar abundance, thereby implying that we may be seeing the early stage of galaxy formation (Lanzetta, Wolfe, & Turnshek 1995). Thus, these deep surveys of high-redshift objects will provide new insight into how disk galaxies were formed and how they have evolved into what we see today.

Compared with the deep realm of the universe, our own Galaxy offers more direct information about the dynamical processes that lead to the formation of disks and halos in galaxies. The space motions of old stellar populations observed at the current epoch retain the "fossil records" of the dynamical state in the early Galaxy, because the relaxation time of these stars exceeds the age of the Galaxy. Since the formation history of these old stars is imprinted in their metal abundances, it is possible to determine how the Galaxy was formed while changing the dynamical state with time.

This avenue of research was pioneered by Eggen, Lynden-Bell, & Sandage (1962, hereafter ELS). In their sample, consisting of nearby disk and high-velocity stars, ELS found a close relationship between orbital motion and metallicity, in the sense that increasingly metal-poor stars have larger orbital eccentricities. This result led them to conclude that the Galaxy collapsed in a free-fall time ($\sim 2 \times 10^8$ yr). Subsequent workers assembled more stellar data based on unbiased sampling and analyzed the data more rigorously (e.g., Yoshii & Saio 1979; Norris, Bessell, & Pickles 1985, hereafter NBP; Norris 1986; Sandage & Fouts 1987; Carney, Latham, & Laird 1990; Norris & Ryan 1991; Beers & Sommer-Larsen 1995). From this work an alternative picture has emerged, suggesting that the collapse of the Galaxy occurred slowly, lasting much longer than a free-fall time, say, $\sim 10^9$ yr. This picture is also supported by the large spread (a few gigayears) in the ages of both globular clusters and field halo stars (Searle & Zinn 1978, hereafter SZ; Schuster & Nissen 1989). SZ have especially argued that the Galactic halo was not formed in an ordered collapse, but from the merger or accretion of numerous fragments, such as dwarf-type galaxies.

It has also been made clear that the Galaxy has an intermediate, rapidly rotating disk (the thick disk), having a ver-

[1] Also Research Center for the Early Universe, Faculty of Science, University of Tokyo, Bunkyo-ku, Tokyo 113, Japan.

tical scale height of ~ 1 kpc, compared with ~ 350 pc for the old thin disk (Yoshii 1982; Yoshii, Ishida, & Stobie 1987; Gilmore & Reid 1983). The thick disk is usually considered to dominate stars in the range [Fe/H] $= -0.6$ to -1 (Freeman 1987), but whether it has a significant metal-weak tail down to [Fe/H] $= -2.0$ is a current topic related to this extra disk component (see, e.g., Morrison, Flynn, & Freeman 1990, hereafter MFF; Beers & Sommer-Larsen 1995).

These kinematic approaches require, among other things, reliable three-dimensional positions and velocities of stars. In an effort to diminish any systematic errors in these basic quantities, the *Hipparcos* satellite was launched in 1989 for the purpose of obtaining accurate trigonometric parallaxes and proper motions for numerous bright stars distributed over the whole sky. *Hipparcos* is characterized by its high accuracy in astrometric measurements, to a level of ~ 1 mas for parallaxes and ~ 1 mas yr^{-1} for proper motions (ESA 1997).

Here we revisit the kinematics of red giants and RR Lyrae stars in the solar neighborhood. The astrometric observations of these stars were parts of the *Hipparcos* program assigned to the senior author's proposals, submitted in 1982. A majority of the stars in the sample are characterized by their low metallicities, [Fe/H] < -1, and are thus thought to represent the old halo population in the Galaxy. Although this sample constitutes only a small subset of all halo stars, it offers the great advantage of having the highest accuracy proper-motion data ever measured by *Hipparcos*. Therefore this sample, combined with a number of well-calibrated photometric and spectroscopic determinations of metal abundances, radial velocities, and distances, may allow us to elucidate a more precise picture of the early evolution of the Galactic halo.

In § 2, we describe the selection of our sample stars for the *Hipparcos* observations together with other available data, such as metal abundances and radial velocities. The qualities of the obtained astrometric data are examined, and the effects of the accuracy of the observations on the resulting kinematics of the stars are discussed. Section 3 is devoted to the kinematic properties of the sample stars and an exploration of whether there is a signature of the metal-weak thick disk that has recently been discussed. Section 4 discusses the orbital motions of the sample stars using a model gravitational potential for the Galaxy. We present the distribution of orbital eccentricities as a function of metallicity and use it as a tool for discriminating the halo from the metal-weak tail of the thick disk. In § 5, we examine whether a large-scale metallicity gradient exists in the Galaxy. The results of the present paper are summarized, and their implications for the formation and evolution of the Galaxy are discussed, in § 6.

2. DATA

2.1. *Star Selection*

Red giants used in this paper were selected from the kinematically unbiased sample of metal-deficient red giants surveyed by Bond (1980), and RR Lyrae stars from the catalogs of variable stars compiled by Kukarkin et al. (1969–1976). The sample stars, originally containing 125 red giants and 362 RR Lyrae stars, were proposed for observation by the *Hipparcos* astrometry satellite by one of the authors in 1982.

Our sample of red giants consists of stars with apparent V magnitudes brighter than $m_V = 12$ mag and metal abundances lower than [Fe/H] $= -1.5$. The Bond survey is essentially complete to this magnitude, although the metal abundances of some of these stars have been significantly revised in subsequent studies, as described below. Our sample of RR Lyrae stars consists of almost all stars with $m_V \leq 12.5$ mag in the Kukarkin catalogs. All 125 red giants, and 173 of the 362 RR Lyrae stars, were ultimately observed with *Hipparcos*.

In order to analyze the three-dimensional motions of these stars as a function of metal abundance, data on photometric distances, radial velocities, and metal abundances were assembled from a number of published works. At the time of this writing, a complete set of such data was available for 122 red giants and 124 RR Lyrae stars in our *Hipparcos* sample.

Combining these available data with the *Hipparcos* measurements of parallaxes and proper motions, we compiled the data set tabulated in Table 1. The *Hipparcos* numbers and the common names of our program stars are listed in columns (1) and (2), respectively. The observed values of the various quantities, together with their standard 1 σ errors, are tabulated in columns (3)–(10). Code numbers for the literature references are given in column (11) for "DA" (photometric distances and metal abundances), "V" (radial velocities), and "P" (ground-based proper motions); their correspondence is summarized in Table 2.

2.2. *Parallaxes and Proper Motions*

The trigonometric parallaxes π and proper-motion components ($\mu_{\alpha*} = \mu_\alpha \cos \delta$, μ_δ) were measured at catalog epoch J1991.25 with *Hipparcos*, and their values for our program stars are listed in columns (3)–(5) of Table 1, together with the errors (typically ~ 1 mas for π and ~ 1 mas yr^{-1} for μ).

We note that a majority of the stars are located farther than 100 pc from the Sun, and the relative errors σ_π/π are greater than 10% in the *Hipparcos* measurements of parallaxes. In particular, for very distant stars for which the true parallaxes are much smaller than their errors, negative values have been assigned to the observed parallaxes. In order to illustrate the systematic errors relevant to the *Hipparcos* observations of our program stars, we show in Figure 1 the relation between σ_π/π and π for the red giants and RR Lyrae stars. It appears that log (σ_π/π) decreases linearly with log π, and this relation virtually agrees with that found for more than 107,000 stars acquired from the first 30 months' observations with *Hipparcos* (Perryman et al. 1995). Thus, the large values of σ_π/π for our sample stars are consistent with the general trend of *Hipparcos*'s accuracy and are not the result of some peculiarity inherent in red giant or RR Lyrae stars. Nevertheless, in order to take advantage of the *Hipparcos* parallax measurements, we adopt the direct determinations of distances for our program stars provided that the relative errors σ_π/π are less than 20%. This condition is fulfilled for only five red giants (HIC 5445, 5458, 29992, 68594, 92167) and one RR Lyrae star (HIC 95497). For the other stars, we use the photometric distances.

Prior to the launch of *Hipparcos*, various ground-based observations had measured proper motions for many of our program stars. We list these ground-based proper motions, where available, in columns (9) and (10) of Table 1. These proper motions are taken from those listed in the Hipparcos

TABLE 1

PROGRAM STARS

Star (HIC) (1)	Other Name (2)	π (mas) (3)	$\mu_{\alpha*}$ (mas yr^{-1}) (4)	μ_{δ} (mas yr^{-1}) (5)	D (kpc) (6)	[Fe/H] (dex) (7)	V_{rad} (km s^{-1}) (8)	$\mu_{\alpha*}^{old}$ (arcsec yr^{-1}) (9)	μ_{δ}^{old} (arcsec yr^{-1}) (10)	References[a] (DA/V/P) (11)
					Red Giants					
434	HD 20	1.40 ± 1.32	130.26 ± 1.68	−41.05 ± 0.87	0.458 ± 0.037	−1.66 ± 0.16	−57.40 ± 0.20	0.154	−0.036	1/2/2
484	HD 97	−0.26 ± 1.41	−25.09 ± 1.73	−178.78 ± 0.68	0.475 ± 0.038	−1.38 ± 0.16	76.30 ± 0.80	−0.026	−0.167	1/2/1
1298	CD −23°72	0.86 ± 1.58	14.05 ± 1.87	−24.04 ± 0.91	0.551 ± 0.044	−1.12 ± 0.16	20.20 ± 0.60	0.012	−0.009	1/2/1
2413	HD 2665	2.11 ± 0.91	40.22 ± 0.81	−64.06 ± 0.62	0.236 ± 0.019	−1.87 ± 0.17	−378.50 ± 1.50	0.041	−0.058	1s/1/2
2463	HD 2796	−0.06 ± 1.06	−2.58 ± 1.18	−52.72 ± 0.71	0.721 ± 0.058	−2.35 ± 0.04	−60.50 ± 0.90	0.001	−0.034	1s/1/1
2618	HD 3008	2.88 ± 1.46	15.17 ± 1.50	−8.24 ± 1.03	1.541 ± 0.123	−1.87 ± 0.01	−80.80 ± 1.10	0.012	−0.010	1s/2/1
2727	HD 3179	2.96 ± 1.56	38.37 ± 1.66	−37.68 ± 1.09	0.593 ± 0.047	−0.92 ± 0.16	−74.50 ± 0.20	0.041	−0.030	1/2/1
3554	HD 4306	4.81 ± 1.40	60.40 ± 1.44	21.00 ± 0.92	0.564 ± 0.045	−2.72 ± 0.14	−67.00 ± 1.20	0.058	0.027	1s/1/1
3635	CD −38°245	−2.31 ± 3.10	13.63 ± 3.13	−8.56 ± 2.35	3.339 ± 0.267	−4.00 ± 0.22	46.60 ± 0.70	...	...	1s/2/...
3770	BD −11°145	1.56 ± 2.39	0.54 ± 2.32	−25.63 ± 1.44	1.855 ± 0.148	−2.02 ± 0.16	−93.40 ± 0.80	−0.005	−0.022	1/2/1
4343	HD 5426	0.17 ± 1.60	25.03 ± 1.53	−55.08 ± 1.04	0.720 ± 0.058	−2.33 ± 0.16	27.70 ± 0.80	−0.037	−0.026	1/2/2
4458	BD −20°170	1.05 ± 1.74	25.54 ± 1.73	−5.48 ± 1.11	0.763 ± 0.061	−1.31 ± 0.16	−5.30 ± 0.40	0.026	0.003	1/2/1
4585	CD −30°298	1.06 ± 2.23	67.31 ± 2.49	24.26 ± 1.77	0.996 ± 0.080	−3.09 ± 0.00	29.70 ± 0.70	...	...	1s/2/...
4933	HD 6268	1.94 ± 1.05	−30.98 ± 1.13	−34.14 ± 1.05	0.671 ± 0.054	−2.37 ± 0.12	40.10 ± 0.60	−0.022	−0.041	1s/1/2
5445	HD 6755	7.74 ± 0.91	627.89 ± 0.65	77.84 ± 0.64	0.170 ± 0.014	−1.62 ± 0.05	−328.70 ± 1.30	0.630	0.074	1s/1/2
5458	HD 6833	4.35 ± 0.77	20.69 ± 0.56	35.28 ± 0.47	0.310 ± 0.025	−1.06 ± 0.31	−245.00 ± 5.00	0.021	0.030	2s/8/2
6710	HD 8724	3.04 ± 0.95	53.29 ± 0.91	−76.32 ± 0.65	0.732 ± 0.059	−1.76 ± 0.00	−110.15 ± 0.15	0.049	−0.075	1s/4,8/2
6894	HD 9051	0.58 ± 1.29	52.58 ± 1.22	−16.58 ± 0.75	0.449 ± 0.036	−1.50 ± 0.16	−72.70 ± 0.50	0.052	−0.018	1/2/2
7553	BD −18°271	−1.33 ± 1.54	7.59 ± 1.44	−25.48 ± 1.19	2.376 ± 0.190	−2.06 ± 0.00	−209.30 ± 1.20	0.005	−0.022	1s/2/1
10497......	HD 13979	1.93 ± 1.25	29.78 ± 1.11	−47.67 ± 0.91	0.803 ± 0.064	−2.63 ± 0.01	54.00 ± 1.10	0.030	−0.063	1s/1/2
11023......	BD −22°395	4.25 ± 1.93	36.76 ± 1.67	−31.43 ± 1.29	1.688 ± 0.135	−2.14 ± 0.16	103.10 ± 1.10	0.038	−0.028	1/2/1
12978......	BD −10°548	1.95 ± 1.98	77.93 ± 1.81	−11.59 ± 2.15	0.831 ± 0.066	−1.71 ± 0.16	238.70 ± 1.00	0.078	−0.009	1/2/1
13044......	CD −36°1052	0.07 ± 1.47	2.34 ± 1.02	10.28 ± 1.18	0.720 ± 0.058	−2.19 ± 0.16	306.00 ± 5.00	0.015	0.013	1/3/2
13749......	CD −30°1121	2.07 ± 1.74	31.11 ± 1.40	−28.51 ± 1.43	0.776 ± 0.062	−1.82 ± 0.16	103.90 ± 0.70	0.032	−0.008	1/2/2
15709......	HD 21022	0.58 ± 1.20	31.13 ± 0.79	−32.51 ± 1.07	1.186 ± 0.095	−1.99 ± 0.16	110.00 ± 3.00	0.036	−0.027	1/3,8/2
16214......	HD 21581	4.27 ± 1.20	65.67 ± 1.41	−77.89 ± 1.04	0.390 ± 0.031	−1.74 ± 0.00	154.20 ± 0.50	0.071	−0.073	1s/2/2
17001......	CD −24°1782	4.42 ± 1.75	78.76 ± 1.08	−124.18 ± 1.31	0.730 ± 0.058	−2.37 ± 0.05	118.50 ± 3.50	...	...	1s/3,8/2
17639......	HD 23798	0.71 ± 0.95	18.83 ± 0.64	−1.44 ± 0.75	1.057 ± 0.085	−1.90 ± 0.16	89.50 ± 0.70	0.020	−0.009	1/3/2
18995......	HD 25532	4.39 ± 1.25	90.45 ± 1.86	−116.79 ± 1.24	0.274 ± 0.022	−1.23 ± 0.00	−112.50 ± 1.20	0.095	−0.119	1s/5/1
19378......	HD 26297	1.28 ± 1.01	43.89 ± 1.04	−4.90 ± 0.79	0.620 ± 0.050	−1.76 ± 0.13	13.50 ± 0.60	0.046	−0.003	1s/1/2
19701......	BD +06°648	2.58 ± 1.25	28.45 ± 1.31	−39.53 ± 1.16	1.252 ± 0.100	−2.04 ± 0.03	−141.40 ± 0.10	0.032	−0.045	1s/1/2
20454......	HD 27928	2.36 ± 1.16	26.90 ± 0.90	−67.47 ± 1.22	0.640 ± 0.051	−2.25 ± 0.16	15.10 ± 0.70	0.000	−0.056	1/3/2
21648......	HD 29574	0.66 ± 1.03	−14.04 ± 0.92	−54.99 ± 0.93	1.165 ± 0.093	−1.55 ± 0.00	23.80 ± 1.00	−0.010	−0.050	1s/1/1
21814......	HD 30229	0.93 ± 0.89	28.49 ± 0.89	−40.92 ± 1.10	0.606 ± 0.048	−2.32 ± 0.16	304.10 ± 2.50	0.115	−0.047	1/6/2
23397......	HD 268957	4.07 ± 1.07	29.84 ± 1.12	129.41 ± 1.33	0.572 ± 0.046	−1.63 ± 0.16	172.30 ± 0.30	0.042	0.116	1/4,8/2
25916......	HD 36702	0.68 ± 0.78	4.35 ± 0.81	−16.93 ± 0.85	1.125 ± 0.090	−1.86 ± 0.16	121.80 ± 0.70	−0.007	−0.016	1/3/2
26040......	HD 274939	2.88 ± 1.06	10.95 ± 1.23	−121.94 ± 1.20	0.472 ± 0.038	−1.67 ± 0.16	190.00 ± 12.00	0.018	−0.130	1/1/2
29992......	HD 44007	5.17 ± 1.02	81.40 ± 1.05	−40.63 ± 0.93	0.155 ± 0.012	−1.61 ± 0.00	165.30 ± 1.65	0.099	−0.035	1s/3,5,8/2
38621......	HD 63791	1.75 ± 1.00	−45.98 ± 0.64	−87.47 ± 0.61	0.470 ± 0.038	−2.00 ± 0.16	−108.20 ± 0.40	−0.039	−0.094	2/2/2
43228......	HD 74462	1.55 ± 1.16	54.08 ± 0.56	−93.61 ± 0.82	0.788 ± 0.063	−1.53 ± 0.07	−168.10 ± 1.20	0.053	−0.104	1s/5/1
46822......	HD 82590	2.39 ± 1.33	34.84 ± 1.86	−125.37 ± 0.87	0.528 ± 0.042	−1.85 ± 0.16	215.60 ± 0.80	0.064	−0.112	1/3/2
47139......	HD 83212	1.96 ± 0.98	−15.51 ± 0.92	−20.41 ± 0.65	0.683 ± 0.055	−1.49 ± 0.10	109.50 ± 0.50	−0.014	−0.012	1s/3/1
47599......	HD 233666	1.22 ± 1.20	13.79 ± 1.17	−28.76 ± 0.70	0.531 ± 0.042	−1.65 ± 0.00	−65.50 ± 0.40	0.014	−0.027	1s/1/1
48019......	HD 84903	−0.37 ± 0.94	−19.04 ± 0.66	−4.31 ± 0.77	0.862 ± 0.069	−2.55 ± 0.16	79.00 ± 5.00	−0.012	0.001	1/3/2
48444......	HD 237846	0.02 ± 1.61	2.07 ± 1.07	−9.62 ± 0.90	0.819 ± 0.066	−2.67 ± 0.16	−302.80 ± 0.80	0.003	−0.002	1s/1/1
48516......	HD 85773	4.07 ± 1.30	−17.97 ± 1.45	−21.79 ± 1.03	1.822 ± 0.146	−2.18 ± 0.04	148.80 ± 1.00	−0.015	−0.011	1s/1/1
50173......	HD 88609	0.63 ± 1.14	2.19 ± 0.98	−31.64 ± 0.69	1.012 ± 0.081	−2.69 ± 0.19	−36.20 ± 0.80	0.003	−0.021	1s/1/1
52297......	CD −30°8626	2.09 ± 1.38	−13.50 ± 0.98	−41.09 ± 1.15	0.728 ± 0.058	−1.67 ± 0.16	262.00 ± 0.70	−0.040	−0.022	1/2/2
52781......	HD 93529	3.70 ± 1.21	−19.85 ± 1.02	−47.42 ± 0.99	0.409 ± 0.033	−1.24 ± 0.16	143.00 ± 0.70	−0.010	−0.040	1/2/2

TABLE 1—*Continued*

Star (HIC) (1)	Other Name (2)	π (mas) (3)	$\mu_{\alpha*}$ (mas yr^{-1}) (4)	μ_δ (mas yr^{-1}) (5)	D (kpc) (6)	[Fe/H] (dex) (7)	V_{rad} (km s^{-1}) (8)	$\mu_{\alpha*}^{old}$ (arcsec yr^{-1}) (9)	μ_δ^{old} (arcsec yr^{-1}) (10)	References[a] (DA/V/P) (11)
55852......	BD +04°2466	−0.96 ± 1.83	−21.38 ± 1.83	−62.58 ± 2.01	0.384 ± 0.031	−1.85 ± 0.00	37.60 ± 1.10	−0.013	−0.045	1s/1/2
57787......	CPD −70°1436	1.68 ± 0.99	−114.39 ± 1.01	13.08 ± 0.82	0.509 ± 0.041	−2.10 ± 0.16	300.00 ± 5.00	...	...	1/3/...
57828......	BD +22°2411	−3.24 ± 1.98	−6.91 ± 1.79	−15.21 ± 1.91	2.229 ± 0.178	−1.95 ± 0.16	34.50 ± 1.90	−0.010	−0.022	1/2/2
57850......	TY Vir	0.72 ± 1.09	−35.15 ± 0.92	−47.34 ± 0.68	0.720 ± 0.058	−1.58 ± 0.00	229.00 ± 1.60	−0.021	−0.041	1s/8/2
57983......	BD −01°2582	2.98 ± 1.35	−21.19 ± 1.34	−117.77 ± 0.78	0.364 ± 0.029	−2.32 ± 0.00	0.20 ± 1.50	−0.025	−0.129	1s/2/1
58139......	HD 103545	0.60 ± 1.23	−49.28 ± 1.41	−37.68 ± 0.90	1.047 ± 0.084	−2.42 ± 0.16	179.70 ± 0.90	−0.054	−0.065	1/2/2
58514......	HD 233891	0.41 ± 1.12	−22.71 ± 0.91	7.88 ± 0.78	0.541 ± 0.043	−1.36 ± 0.00	−45.20 ± 1.50	−0.023	0.016	1s/1/1
58682......	BD +09°2574	−0.53 ± 1.75	−10.11 ± 1.65	−45.77 ± 0.90	1.123 ± 0.090	−1.95 ± 0.16	−48.80 ± 0.60	−0.008	−0.047	1/2/1
58896......	HD 104893	0.15 ± 1.25	−33.14 ± 1.17	−7.75 ± 0.71	1.401 ± 0.112	−1.86 ± 0.00	23.60 ± 0.70	−0.058	−0.033	1s/1/2
59239......	HD 105546	1.96 ± 0.91	−32.02 ± 0.66	−69.24 ± 0.75	0.365 ± 0.029	−1.44 ± 0.00	19.30 ± 1.20	−0.021	−0.070	1s/1/1
59672......	HD 106373	2.22 ± 1.09	−106.52 ± 1.01	21.95 ± 0.59	0.430 ± 0.034	−2.48 ± 0.16	96.00 ± 12.00	−0.090	0.030	1/1/2
60387......	HD 107752	0.46 ± 1.59	−48.63 ± 1.80	−36.86 ± 1.45	1.364 ± 0.109	−2.68 ± 0.00	220.00 ± 1.10	...	...	1s/2/...
60719......	HD 108317	4.53 ± 1.06	−167.62 ± 1.09	−24.87 ± 0.76	0.319 ± 0.026	−2.34 ± 0.08	6.50 ± 1.20	−0.162	−0.026	1s/1/2
60846......	HD 108577	2.35 ± 1.51	−76.22 ± 1.78	−45.78 ± 0.99	1.039 ± 0.083	−2.50 ± 0.16	−111.70 ± 1.00	−0.077	−0.045	1/2/1
60892......	BD +04°2621	0.64 ± 1.97	−20.22 ± 1.82	−34.78 ± 1.20	1.457 ± 0.117	−2.34 ± 0.00	−42.00 ± 1.10	−0.022	−0.032	1s/1/2
61824......	HD 110184	1.00 ± 0.99	−14.65 ± 1.01	−9.11 ± 0.57	1.221 ± 0.098	−2.31 ± 0.08	140.10 ± 0.30	−0.011	−0.023	1s/1/2
61899......	HD 110281	1.74 ± 1.35	6.77 ± 1.12	−31.84 ± 0.81	2.480 ± 0.198	−1.75 ± 0.16	141.60 ± 0.70	0.007	−0.033	1/2/1
62235......	HD 110885	0.01 ± 1.34	−11.31 ± 1.20	−47.74 ± 0.81	0.487 ± 0.039	−1.59 ± 0.16	...	0.000	−0.057	1/.../2
63385......	BD +10°2495	2.36 ± 1.49	−45.25 ± 1.25	31.99 ± 0.99	0.775 ± 0.062	−2.14 ± 0.16	252.90 ± 0.50	−0.043	0.030	1/2/2
63758......	BD +12°2547	3.88 ± 1.64	4.03 ± 1.53	−54.49 ± 1.18	1.473 ± 0.118	−2.07 ± 0.16	5.70 ± 0.10	...	...	1/2/...
64786......	HD 115444	3.55 ± 1.12	5.10 ± 0.91	−60.36 ± 0.87	0.784 ± 0.063	−2.63 ± 0.07	−27.60 ± 5.00	0.010	−0.070	1s/7/2
65852......	BD +03°2782	3.90 ± 1.39	−32.43 ± 1.08	−7.45 ± 1.02	1.750 ± 0.140	−2.30 ± 0.16	32.30 ± 0.10	−0.020	−0.012	2/2/2
66246......	HD 118055	0.66 ± 1.24	−23.09 ± 1.64	−14.69 ± 0.94	1.129 ± 0.090	−1.76 ± 0.00	−101.00 ± 0.30	−0.020	−0.010	1s/3/1
66378......	BD +18°2757	0.28 ± 1.37	−16.19 ± 1.27	−27.84 ± 1.02	1.343 ± 0.107	−2.52 ± 0.16	−22.20 ± 5.40	−0.019	−0.032	1/2/1
66959......	HD 119516	0.05 ± 1.39	−50.51 ± 1.32	−13.77 ± 1.10	0.507 ± 0.041	−2.49 ± 0.16	−287.00 ± 0.70	−0.052	−0.034	1/2/2
67822......	HD 121135	1.73 ± 1.29	−33.70 ± 1.06	−18.81 ± 0.78	0.869 ± 0.070	−1.83 ± 0.16	126.40 ± 0.50	−0.047	−0.017	1/2/2
67964......	HD 121261	1.09 ± 1.47	−35.89 ± 1.79	−11.86 ± 1.32	1.301 ± 0.104	−1.52 ± 0.16	99.40 ± 0.20	−0.053	−0.031	1/3/2
68594......	HD 122563	3.76 ± 0.72	−188.93 ± 0.56	−70.10 ± 0.39	0.308 ± 0.025	−2.55 ± 0.10	−24.80 ± 0.00	−0.192	−0.074	1s/4/2
68807......	HD 122956	3.30 ± 0.88	−94.10 ± 0.95	−44.13 ± 0.72	0.356 ± 0.028	−1.74 ± 0.14	166.30 ± 0.40	−0.095	−0.041	1s/3/2
69468......	BD +09°2860	4.97 ± 2.22	11.62 ± 2.32	−43.43 ± 1.65	1.043 ± 0.083	−1.67 ± 0.16	−19.00 ± 0.30	...	...	1/2/...
69470......	HD 124358	1.16 ± 1.52	−94.27 ± 1.94	−27.96 ± 1.37	1.128 ± 0.090	−1.98 ± 0.16	325.00 ± 0.60	−0.095	−0.024	1/3/1
69525......	CD −37°9248	1.32 ± 1.47	−14.51 ± 1.24	−11.66 ± 0.98	1.140 ± 0.091	...	258.00 ± 2.00	−0.023	−0.012	2/8/2
69746......	BD +09°2870	2.24 ± 1.58	−56.48 ± 1.45	3.13 ± 1.08	1.347 ± 0.108	−2.39 ± 0.00	−120.70 ± 0.70	−0.057	0.000	1s/2/2
70199......	BD +01°2916	1.47 ± 1.53	−23.62 ± 1.35	−13.79 ± 1.23	1.919 ± 0.154	−1.61 ± 0.00	−12.70 ± 1.10	−0.021	−0.008	1s/1/1
70381......	BD +08°2856	−0.47 ± 1.83	10.32 ± 1.51	−21.41 ± 1.39	2.454 ± 0.196	−2.02 ± 0.00	64.50 ± 0.30	0.009	−0.018	1s/2/2
70519......	HD 126238	3.81 ± 0.95	25.31 ± 0.69	−105.50 ± 0.68	0.241 ± 0.019	−1.85 ± 0.00	247.00 ± 5.00	0.037	−0.100	1s/3/2
70647......	HD 126587	1.40 ± 1.44	−15.97 ± 1.22	−53.02 ± 1.12	0.621 ± 0.050	−2.79 ± 0.00	149.20 ± 0.60	−0.013	−0.046	1s/1/1
71087......	BD +18°2890	1.52 ± 1.45	−14.09 ± 1.05	−99.78 ± 1.07	0.930 ± 0.074	−2.00 ± 0.16	−22.60 ± 5.30	...	...	2/2/...
71458......	HD 128279	5.96 ± 1.32	64.57 ± 1.79	−344.92 ± 1.10	0.158 ± 0.013	−2.22 ± 0.02	−81.65 ± 4.35	0.052	−0.318	1s/3,8/2
73960......	BD +30°2611	3.45 ± 1.31	15.45 ± 1.11	−8.71 ± 1.04	1.114 ± 0.089	−1.26 ± 0.07	−278.20 ± 1.20	0.011	−0.006	1s/5/1
74003......	BD +18°2976	2.31 ± 1.71	−29.82 ± 2.11	−33.36 ± 1.76	1.687 ± 0.135	−2.42 ± 0.16	−173.10 ± 1.60	−0.039	−0.039	1/2/2
74491......	HD 135148	−2.11 ± 1.37	−27.84 ± 1.00	3.03 ± 1.07	1.111 ± 0.089	−1.88 ± 0.03	−91.90 ± 4.40	−0.024	0.001	1s/2/2
74717......	HD 135449	5.45 ± 1.35	−131.72 ± 1.21	−41.67 ± 1.20	0.450 ± 0.036	−1.47 ± 0.16	−23.00 ± 12.00	−0.134	−0.063	1/1/2
75221......	HD 136316	1.08 ± 0.95	−27.55 ± 0.86	−64.44 ± 0.83	0.496 ± 0.040	−2.00 ± 0.14	−45.00 ± 12.00	−0.032	−0.064	1s/1/2
75263......	BD +01°3070	2.40 ± 2.17	−35.92 ± 1.67	65.36 ± 1.40	0.502 ± 0.040	−1.85 ± 0.16	−329.40 ± 2.90	−0.035	0.057	1/2/2
77483......	HD 141531	3.16 ± 1.76	−15.12 ± 2.33	−55.99 ± 2.37	1.292 ± 0.103	−1.57 ± 0.16	2.60 ± 0.90	−0.015	−0.056	1/2/1
77739......	BD +05°3098	2.48 ± 2.31	−44.38 ± 2.57	−55.22 ± 2.88	1.235 ± 0.099	−2.40 ± 0.16	−160.50 ± 0.80	...	...	1/2/...
80822......	BD +11°2998	3.25 ± 1.23	−108.58 ± 1.27	−55.90 ± 1.24	0.425 ± 0.034	−1.22 ± 0.16	50.20 ± 0.40	−0.121	−0.060	1s/2/2
81078......	BD +09°3223	1.88 ± 1.41	−33.97 ± 1.29	−106.62 ± 1.19	0.501 ± 0.040	−2.41 ± 0.16	67.00 ± 0.80	...	...	1/2/...
85487......	BD +17°3248	3.67 ± 1.50	−45.90 ± 0.96	−22.93 ± 1.26	0.510 ± 0.041	−2.07 ± 0.16	−145.60 ± 0.50	−0.046	−0.023	1/1/2
88527......	HD 165195	2.20 ± 1.04	−28.55 ± 0.83	−82.87 ± 0.68	0.646 ± 0.052	−2.42 ± 0.11	−0.20 ± 5.00	−0.019	−0.081	1s/1/2
88977......	HD 166161	3.25 ± 1.19	−98.22 ± 1.20	−191.08 ± 0.73	0.197 ± 0.016	−1.27 ± 0.05	68.40 ± 0.30	−0.100	−0.193	1s/1/2
91182......	HD 171496	5.57 ± 1.35	−9.37 ± 1.60	3.21 ± 1.05	0.246 ± 0.020	−1.16 ± 0.16	...	...	...	1/.../...

TABLE 1—*Continued*

Star (HIC) (1)	Other Name (2)	π (mas) (3)	$\mu_{\alpha*}$ (mas yr^{-1}) (4)	μ_{δ} (mas yr^{-1}) (5)	D (kpc) (6)	[Fe/H] (dex) (7)	V_{rad} (km s^{-1}) (8)	$\mu_{\alpha*}^{old}$ (arcsec yr^{-1}) (9)	μ_{δ}^{old} (arcsec yr^{-1}) (10)	References[a] (DA/V/P) (11)
92167	HD 175305	6.18 ± 0.56	319.24 ± 0.56	79.89 ± 0.57	0.115 ± 0.009	−1.54 ± 0.00	−181.00 ± 2.50	0.315	0.082	1s/5/2
96248	HD 184266	3.28 ± 0.95	129.91 ± 0.87	−197.33 ± 0.54	0.223 ± 0.018	−1.87 ± 0.16	−348.40 ± 0.20	0.131	−0.201	1/1/2
96508	HD 184711	3.15 ± 1.16	1.42 ± 1.48	−51.12 ± 1.02	1.012 ± 0.081	−2.30 ± 0.09	101.60 ± 0.30	0.000	−0.059	1s/1/2
97192	HD 186478	1.34 ± 1.25	−22.23 ± 1.29	−84.42 ± 0.77	1.025 ± 0.082	−2.45 ± 0.16	30.90 ± 2.40	−0.009	−0.076	1/3/2
97468	HD 187111	1.99 ± 1.09	37.01 ± 1.07	−58.21 ± 0.49	0.615 ± 0.049	−1.95 ± 0.31	−181.00 ± 2.50	0.032	−0.054	1s/1/2
98339	BD −18°5550	1.90 ± 1.44	11.89 ± 1.71	−91.80 ± 0.86	0.740 ± 0.059	−2.84 ± 0.13	−126.20 ± 0.60	0.010	−0.080	1s/3/1
98974	HD 190287	7.12 ± 1.50	−36.32 ± 1.72	−165.27 ± 1.04	0.145 ± 0.012	−1.09 ± 0.16	135.00 ± 3.00	−0.047	−0.179	1/3,8/2
101379......	HD 195636	0.74 ± 1.77	−65.72 ± 1.80	−91.69 ± 1.30	0.592 ± 0.047	−2.82 ± 0.00	−257.80 ± 0.60	−0.062	−0.084	1s/8/1
101740......	BD −17°6036	1.65 ± 2.68	−28.90 ± 2.51	−40.87 ± 2.43	1.272 ± 0.102	−2.70 ± 0.00	19.20 ± 0.50	−0.030	−0.035	1s/2/1
102447......	BD −15°5781	−0.92 ± 2.33	5.54 ± 2.78	−21.41 ± 2.25	1.932 ± 0.155	−2.47 ± 0.16	−76.40 ± 1.00	0.004	−0.014	1/2/1
103337......	BD −14°5890	1.48 ± 1.86	−16.96 ± 2.05	−83.97 ± 1.67	0.930 ± 0.074	−2.01 ± 0.16	117.50 ± 0.90	−0.024	−0.073	1/2/1
104191......	HD 200654	3.20 ± 1.25	191.96 ± 1.34	−274.08 ± 0.85	0.463 ± 0.037	−2.79 ± 0.16	−48.00 ± 4.58	0.203	−0.284	1/3,4,8/2
105993......	BD −03°5215	2.11 ± 2.03	18.48 ± 2.49	−24.54 ± 1.44	0.731 ± 0.058	−1.72 ± 0.00	−293.70 ± 0.60	...	...	1s/2/...
106095......	HD 204543	−0.24 ± 1.38	−0.56 ± 1.58	−47.03 ± 0.94	0.725 ± 0.058	−1.69 ± 0.05	−98.20 ± 0.40	−0.004	−0.041	1s/1/2
107337......	HD 206739	0.69 ± 1.24	41.64 ± 1.43	−31.81 ± 0.87	0.574 ± 0.046	−1.58 ± 0.00	−57.80 ± 1.20	0.042	−0.017	1s/2/1
107428......	BD −09°5831	−0.40 ± 2.12	−0.76 ± 2.10	−17.00 ± 0.97	1.896 ± 0.152	−1.87 ± 0.16	14.50 ± 0.60	−0.004	−0.004	1/2/1
111730......	HD 214362	1.45 ± 1.32	173.41 ± 1.55	−55.79 ± 0.87	0.493 ± 0.039	−2.20 ± 0.16	−92.30 ± 0.30	0.180	−0.045	1/3/1
112796......	HD 216143	3.14 ± 1.20	−68.64 ± 1.45	−105.05 ± 0.88	0.690 ± 0.055	−2.20 ± 0.10	−115.90 ± 0.50	−0.072	−0.093	1s/1/1
114502......	HD 218857	3.51 ± 1.42	−50.35 ± 2.32	−95.11 ± 1.11	0.410 ± 0.033	−2.15 ± 0.16	−169.60 ± 0.40	−0.049	−0.081	1/1/1
115649......	HD 220662	−0.27 ± 1.87	8.87 ± 2.38	−21.94 ± 1.84	1.874 ± 0.150	−1.59 ± 0.00	−78.10 ± 0.80	0.010	−0.010	1s/2/2
115771......	HD 220838	−2.23 ± 1.38	1.26 ± 1.65	−12.43 ± 1.17	1.426 ± 0.114	−1.72 ± 0.00	−22.80 ± 0.10	0.023	−0.060	1s/2/2
115949......	HD 221170	2.30 ± 0.84	−15.91 ± 0.62	−54.57 ± 0.51	0.689 ± 0.055	−2.01 ± 0.08	−121.90 ± 0.60	−0.018	−0.048	1s/2/1
116825......	HD 222434	0.06 ± 1.27	−0.84 ± 1.18	−45.25 ± 1.13	0.974 ± 0.078	−1.56 ± 0.16	13.40 ± 0.70	−0.036	−0.028	1/2/2
					RR Lyrae Stars					
226.........	RU Scl	0.63 ± 1.67	54.29 ± 2.14	−17.92 ± 1.02	0.791 ± 0.047	−1.25 ± 0.13	38.00 ± 8.00	0.056	−0.020	3/9/3
320.........	UU Cet	6.48 ± 4.13	33.37 ± 4.84	−0.43 ± 1.88	1.792 ± 0.110	−1.32 ± 0.20	−114.00 ± 3.00	0.027	−0.006	4/9/1
1182	UY Scl	4.81 ± 3.12	18.30 ± 2.64	4.76 ± 2.31	...	...	...	...	...	.../.../...
1222	V363 Cas	2.16 ± 1.67	−1.54 ± 1.62	−2.27 ± 1.48	...	...	...	...	...	.../.../...
1878	SW And	−0.04 ± 1.50	−5.09 ± 1.49	−19.21 ± 1.00	0.537 ± 0.016	−0.38 ± 0.17	−21.00 ± 2.00	0.005	−0.025	3/9/1
2655	RX Cet	2.70 ± 2.63	−20.19 ± 3.42	−62.68 ± 1.89	1.373 ± 0.091	−1.46 ± 0.09	−58.00 ± 7.00	−0.029	−0.062	3/9/1
4541	W Tuc	4.88 ± 1.82	4.62 ± 1.65	−20.25 ± 1.79	1.465 ± 0.106	−1.64 ± 0.17	63.00 ± 3.00	0.003	0.002	3/9/3
4725	RU Cet	3.02 ± 3.17	20.36 ± 3.56	−27.45 ± 2.02	1.571 ± 0.112	−1.60 ± 0.12	57.00 ± 8.00	0.022	−0.010	3/9/1
5803	RU Psc	2.20 ± 1.63	96.20 ± 2.18	−39.82 ± 0.90	...	...	−115.00 ± 0.00	0.099	−0.047	.../9/1
6029	XX And	1.50 ± 2.15	58.97 ± 1.64	−35.46 ± 1.47	0.993 ± 0.085	−2.01 ± 0.07	0.00 ± 5.00	0.035	−0.036	3/9/1
6094	VW Scl	1.66 ± 2.12	25.59 ± 1.91	−38.16 ± 1.29	...	...	...	...	...	.../.../...
6115	AM Tuc	0.22 ± 1.93	23.57 ± 1.85	−27.88 ± 2.12	...	...	130.00 ± 0.00	...	...	.../9/...
6301	SS Psc	3.81 ± 2.05	0.22 ± 1.95	−2.89 ± 1.22	...	...	5.00 ± 0.00	−0.007	0.004	.../9/1
7149	RR Cet	−0.03 ± 1.34	10.55 ± 1.29	−43.98 ± 0.82	0.661 ± 0.045	−1.52 ± 0.12	−75.00 ± 1.00	−0.001	−0.039	3/9/1
7398	VX Scl	−2.35 ± 2.77	37.57 ± 2.17	−24.77 ± 1.61	2.033 ± 0.190	−2.25 ± 0.11	−47.00 ± 11.00	...	...	3/9/...
8163	SV Scl	5.56 ± 2.07	−2.09 ± 1.93	−35.53 ± 1.30	...	...	−10.00 ± 0.00	...	...	.../9/...
8939	CI And	−6.34 ± 4.66	−0.35 ± 3.63	−3.98 ± 2.41	1.663 ± 0.074	−0.83 ± 0.22	99.00 ± 30.00	−0.002	−0.004	3/9/1
9361	XZ Cet	1.65 ± 1.33	30.62 ± 1.25	−7.74 ± 0.98	0.641 ± 0.060	−2.27 ± 0.13	167.00 ± 10.00	0.041	−0.001	3/9/1
9932	SS For	3.56 ± 1.44	28.42 ± 1.22	−71.48 ± 1.14	0.770 ± 0.048	−1.35 ± 0.24	−112.00 ± 1.00	0.043	−0.072	3/9/3
10491	RV Cet	2.33 ± 2.03	28.71 ± 1.94	−20.68 ± 1.40	1.031 ± 0.064	−1.32 ± 0.09	−93.00 ± 7.00	0.026	−0.018	3/9/1
11517	RZ Cet	−2.57 ± 3.43	21.67 ± 2.62	−0.92 ± 2.88	1.720 ± 0.117	−1.50 ± 0.09	−10.00 ± 6.00	0.026	0.019	3/9/1
12199	CS Eri	3.25 ± 0.97	95.42 ± 0.87	6.92 ± 0.85	...	...	...	0.100	0.005	.../.../1
14601	X Ari	0.89 ± 1.55	66.42 ± 1.94	−88.06 ± 1.73	0.521 ± 0.051	−2.40 ± 0.09	−35.00 ± 3.00	0.060	−0.092	3/9/1
14856	SV Eri	1.22 ± 1.77	12.48 ± 1.79	−51.10 ± 1.95	0.709 ± 0.061	−2.04 ± 0.07	−12.00 ± 9.00	0.015	−0.040	3/9/1
15726	KN Per	6.52 ± 3.49	4.45 ± 3.30	−12.08 ± 2.52	...	...	...	−0.011	−0.011	.../.../1
16321	SX For	−1.23 ± 1.89	35.33 ± 1.62	−9.95 ± 1.73	1.245 ± 0.090	−1.62 ± 0.11	227.00 ± 12.00	...	...	3/9/...

TABLE 1—*Continued*

Star (HIC) (1)	Other Name (2)	π (mas) (3)	$\mu_{\alpha*}$ (mas yr^{-1}) (4)	μ_δ (mas yr^{-1}) (5)	D (kpc) (6)	[Fe/H] (dex) (7)	V_{rad} (km s^{-1}) (8)	$\mu_{\alpha*}^{old}$ (arcsec yr^{-1}) (9)	μ_δ^{old} (arcsec yr^{-1}) (10)	References[a] (DA/V/P) (11)
18548......	EZ Cep	3.26 ± 8.19	−16.72 ± 7.85	27.86 ± 8.69	...	...	...	0.005	0.012	.../.../1
19993......	AR Per	1.84 ± 1.64	−7.01 ± 1.69	−9.63 ± 1.17	0.495 ± 0.015	−0.43 ± 0.20	5.00 ± 1.00	−0.002	0.005	3/9/3
22442......	RX Eri	1.08 ± 1.29	−15.63 ± 1.16	−11.15 ± 1.04	0.609 ± 0.037	−1.30 ± 0.16	66.00 ± 1.00	−0.016	−0.007	3/9/1
22466......	U Pic	1.51 ± 1.65	−1.96 ± 1.56	1.62 ± 2.12	1.265 ± 0.052	−0.73 ± 0.23	30.00 ± 12.00	−0.001	−0.017	3/9/3
22750......	BB Eri	2.66 ± 3.03	31.74 ± 2.52	−1.71 ± 2.44	1.445 ± 0.099	−1.51 ± 0.18	235.00 ± 11.00	0.034	0.009	3/9/1
22943......	V429 Ori	−0.37 ± 1.69	3.02 ± 1.96	4.62 ± 1.28	...	...	...	−0.001	0.012	.../.../1
22952......	U Lep	3.16 ± 1.90	41.43 ± 1.25	−61.32 ± 1.63	1.022 ± 0.084	−1.93 ± 0.15	128.00 ± 11.00	0.043	−0.059	3/9/1
24226......	BH Aur	8.68 ± 3.19	0.74 ± 3.33	−3.20 ± 1.92	...	...	...	...	...	.../.../...
24471......	RY Col	1.20 ± 1.33	34.70 ± 1.17	22.95 ± 1.35	1.061 ± 0.058	−1.11 ± 0.17	482.00 ± 15.00	0.036	0.018	3/9/3
28699......	RW Col	5.94 ± 6.53	1.01 ± 5.51	16.32 ± 7.11	3.235 ± 0.167	−1.03 ± 0.27	150.00 ± 14.00	...	...	3/9/...
29528......	RX Col	−5.15 ± 3.41	7.93 ± 2.62	10.65 ± 3.87	2.370 ± 0.177	−1.70 ± 0.07	356.00 ± 11.00	...	...	3/9/...
34743......	TZ Aur	−1.81 ± 3.57	−12.47 ± 5.18	−8.63 ± 2.90	1.505 ± 0.066	−0.80 ± 0.20	46.00 ± 6.00	−0.003	−0.014	3/9/1
35281......	AA CMi	4.59 ± 3.42	0.55 ± 3.05	3.05 ± 2.20	...	...	...	...	...	.../.../...
35584......	HH Pup	0.89 ± 1.61	2.24 ± 1.73	−0.43 ± 1.81	1.029 ± 0.041	−0.69 ± 0.17	13.00 ± 12.00	...	...	3/9/...
35667......	RR Gem	−4.98 ± 2.83	−1.24 ± 3.80	0.67 ± 2.07	1.114 ± 0.031	−0.35 ± 0.30	64.00 ± 1.00	−0.003	−0.002	3/9/3
36750......	TV Lyn	−2.36 ± 2.80	−7.32 ± 2.96	5.06 ± 2.57	...	...	...	−0.005	0.001	.../.../1
37779......	HK Pup	1.52 ± 2.57	21.12 ± 2.36	0.29 ± 1.19	...	...	...	...	...	.../.../...
37805......	TW Lyn	−3.31 ± 4.18	−6.69 ± 5.08	1.11 ± 3.26	1.633 ± 0.096	−1.23 ± 0.25	−40.00 ± 26.00	0.007	0.009	3/9/1
38361......	BB CMi	0.28 ± 1.94	6.88 ± 2.06	−14.46 ± 1.56	...	...	...	0.005	−0.023	.../.../1
38441......	KZ Pup	6.90 ± 3.44	−0.24 ± 2.37	−4.30 ± 1.64	...	...	...	...	...	.../.../...
38561......	SZ Gem	2.62 ± 3.25	−10.89 ± 3.19	−27.66 ± 2.13	1.599 ± 0.125	−1.81 ± 0.15	307.00 ± 11.00	−0.012	−0.034	3/9/1
39009......	UY Cam	−1.64 ± 2.08	−3.03 ± 1.48	−16.65 ± 1.90	...	...	...	−0.011	−0.014	.../.../1
39849......	XX Pup	1.58 ± 2.41	−19.09 ± 2.03	−2.11 ± 2.13	1.090 ± 0.074	−1.50 ± 0.20	386.00 ± 7.00	−0.031	−0.001	4/9/3
40186......	DD Hya	−1.50 ± 4.50	1.65 ± 5.91	−6.65 ± 3.75	1.882 ± 0.095	−1.00 ± 0.14	153.00 ± 25.00	−0.007	−0.012	3/9/1
40379......	IU Pup	−40.06 ± 24.14	11.79 ± 20.59	5.47 ± 21.63	...	...	...	...	...	.../.../...
41936......	TT Cnc	1.95 ± 3.00	−40.96 ± 3.13	−29.24 ± 2.35	1.262 ± 0.089	−1.58 ± 0.16	49.00 ± 5.00	−0.046	−0.040	3/9/1
42115......	ET Hya	2.31 ± 5.31	18.50 ± 4.18	−13.33 ± 3.83	1.898 ± 0.141	−1.69 ± 0.15	320.00 ± 20.00	−0.017	−0.007	3/9/1
44428......	TT Lyn	−2.06 ± 1.67	−81.96 ± 1.57	−41.83 ± 0.98	0.714 ± 0.055	−1.76 ± 0.20	−67.00 ± 1.00	−0.084	−0.040	4/9/1
45292......	SZ Hya	−0.43 ± 24.44	14.44 ± 27.29	−61.56 ± 20.99	1.321 ± 0.101	−1.75 ± 0.08	140.00 ± 9.00	−0.007	−0.038	3/9/1
45709......	RW Cnc	−4.78 ± 3.06	1.50 ± 3.22	−33.33 ± 1.78	1.731 ± 0.119	−1.52 ± 0.24	−85.00 ± 7.00	0.008	−0.042	3/9/1
47796......	CD Vel	8.43 ± 3.26	−39.01 ± 3.38	23.65 ± 3.58	...	...	...	...	...	.../.../...
48503......	T Sex	2.38 ± 1.72	−21.08 ± 1.98	−22.43 ± 0.85	...	...	10.00 ± 0.00	−0.015	−0.022	.../9/1
49628......	RR Leo	−0.54 ± 2.18	−16.97 ± 2.51	−9.34 ± 1.52	0.988 ± 0.069	−1.57 ± 0.19	88.00 ± 1.00	−0.017	−0.013	3/9/1
50073......	WZ Hya	2.90 ± 2.46	−8.69 ± 2.82	−14.78 ± 1.79	0.947 ± 0.058	−1.30 ± 0.19	304.00 ± 8.00	0.001	−0.015	3/9/1
50289......	WY Ant	0.00 ± 1.67	35.64 ± 1.56	−48.74 ± 1.56	1.025 ± 0.075	−1.66 ± 0.20	211.00 ± 24.00	0.026	−0.048	3/9/3
53213......	AF Vel	2.24 ± 2.13	40.68 ± 1.51	−13.96 ± 1.56	1.062 ± 0.077	−1.64 ± 0.20	236.00 ± 16.00	0.059	−0.018	4/9/3
54694......	BI Hya	1.23 ± 1.75	−19.17 ± 1.66	5.76 ± 1.23	...	...	...	...	...	.../.../...
55825......	W Crt	−0.27 ± 2.62	−22.26 ± 2.52	−8.02 ± 1.78	1.293 ± 0.043	−0.50 ± 0.16	65.00 ± 13.00	−0.024	−0.015	3/9/1
56088......	TU UMa	−0.03 ± 1.35	−68.91 ± 1.18	−52.47 ± 1.04	0.680 ± 0.045	−1.44 ± 0.16	88.00 ± 1.00	−0.076	−0.050	3/9/1
56350......	AX Leo	7.89 ± 5.37	−26.49 ± 6.74	−27.13 ± 4.81	2.146 ± 0.203	−2.28 ± 0.23	182.00 ± 10.00	−0.019	−0.021	3/9/1
56409......	SS Leo	1.12 ± 2.25	−24.48 ± 2.12	−25.00 ± 1.68	1.221 ± 0.097	−1.83 ± 0.14	163.00 ± 3.00	−0.024	−0.028	3/9/1
56734......	SU Dra	1.11 ± 1.15	−46.30 ± 0.97	−77.87 ± 1.01	0.693 ± 0.053	−1.74 ± 0.14	−167.00 ± 1.00	−0.049	−0.073	3/9/1
56742......	BX Leo	2.79 ± 3.23	−24.23 ± 3.80	−15.50 ± 2.87	...	...	...	−0.026	−0.011	.../.../1
56785......	ST Leo	−2.33 ± 2.75	−11.23 ± 3.05	−38.21 ± 2.07	1.374 ± 0.083	−1.29 ± 0.22	153.00 ± 4.00	−0.006	−0.034	3/9/1
57625......	X Crt	−0.31 ± 2.58	−1.17 ± 2.07	−41.63 ± 1.58	1.517 ± 0.116	−1.75 ± 0.17	79.00 ± 4.00	−0.001	−0.036	3/9/1
57812......	V753 Cen	2.91 ± 1.82	16.67 ± 1.44	−39.96 ± 1.29	...	...	...	...	...	.../.../...
59208......	UU Vir	−0.37 ± 1.97	−44.42 ± 2.06	−4.65 ± 1.55	0.896 ± 0.040	−0.82 ± 0.20	−8.00 ± 1.00	−0.030	−0.004	3/9/3
59411......	AB UMa	0.91 ± 1.90	−18.50 ± 1.72	−15.42 ± 1.50	0.995 ± 0.041	−0.72 ± 0.59	−56.00 ± 26.00	−0.013	−0.020	3/9/1
59946......	SW Dra	0.21 ± 1.15	−25.59 ± 1.04	−8.81 ± 0.98	0.894 ± 0.053	−1.24 ± 0.07	−30.00 ± 1.00	−0.032	−0.009	3/9/1
61029......	UZ CVn	16.26 ± 7.16	−11.53 ± 4.78	−39.45 ± 5.96	2.072 ± 0.200	−2.34 ± 0.14	−38.00 ± 26.00	0.001	−0.023	3/9/1
61031......	SV Hya	5.57 ± 2.06	−36.23 ± 1.78	12.97 ± 1.59	0.825 ± 0.062	−1.70 ± 0.27	100.00 ± 8.00	−0.055	0.008	3/9/3
61225......	S Com	−1.34 ± 2.67	−16.44 ± 3.43	−16.52 ± 2.15	1.594 ± 0.136	−2.00 ± 0.20	−55.00 ± 4.00	−0.022	−0.020	3/9/1

TABLE 1—*Continued*

Star (HIC) (1)	Other Name (2)	π (mas) (3)	$\mu_{\alpha*}$ (mas yr^{-1}) (4)	μ_{δ} (mas yr^{-1}) (5)	D (kpc) (6)	[Fe/H] (dex) (7)	V_{rad} (km s^{-1}) (8)	$\mu_{\alpha*}^{old}$ (arcsec yr^{-1}) (9)	μ_{δ}^{old} (arcsec yr^{-1}) (10)	References[a] (DA/V/P) (11)
61809......	U Com	3.46 ± 2.75	−44.45 ± 3.62	−13.75 ± 1.98	...	...	...	−0.052	−0.019	.../.../1
63054......	AT Vir	1.87 ± 2.28	−61.31 ± 1.99	−23.11 ± 1.42	1.375 ± 0.113	−1.91 ± 0.21	346.00 ± 8.00	−0.054	−0.018	3/9/1
64875......	ST Com	−5.17 ± 2.71	−23.97 ± 2.77	−33.98 ± 1.56	1.350 ± 0.080	−1.26 ± 0.20	−68.00 ± 7.00	−0.036	−0.036	4/9/3
65063......	AV Vir	3.02 ± 3.02	9.56 ± 2.96	−38.69 ± 1.97	1.664 ± 0.103	−1.32 ± 0.30	152.00 ± 4.00	0.006	−0.034	3/9/1
65344......	AM Vir	−3.25 ± 2.91	2.57 ± 2.71	−44.07 ± 1.59	1.384 ± 0.091	−1.45 ± 0.11	99.00 ± 24.00	−0.002	−0.052	3/9/1
65445......	AU Vir	−0.21 ± 2.95	−5.72 ± 2.78	−26.47 ± 1.90	...	...	130.00 ± 0.00	−0.008	−0.026	.../9/1
65547......	SX UMa	0.70 ± 1.39	−67.24 ± 1.18	2.49 ± 1.41	...	...	−135.00 ± 0.00	−0.067	0.002	.../9/1
66122......	RV UMa	0.66 ± 1.43	−26.33 ± 1.53	−43.32 ± 1.52	1.031 ± 0.059	−1.19 ± 0.16	−183.00 ± 9.00	−0.028	−0.047	3/9/1
67087......	RZ CVn	−1.75 ± 2.45	−53.42 ± 2.41	−0.15 ± 1.60	1.503 ± 0.124	−1.92 ± 0.32	−12.00 ± 7.00	−0.058	−0.004	3/9/1
67227......	RV Oct	0.42 ± 1.39	−32.99 ± 1.14	15.59 ± 1.37	0.969 ± 0.060	−1.34 ± 0.25	134.00 ± 20.00	...	...	3/9/...
67354......	SS CVn	−1.69 ± 2.62	6.34 ± 1.47	−42.80 ± 1.69	1.788 ± 0.123	−1.52 ± 0.23	−15.00 ± 22.00	0.012	−0.051	3/9/1
67653......	BB Vir	1.02 ± 2.53	−49.65 ± 2.26	−3.51 ± 1.62	1.238 ± 0.089	−1.61 ± 0.20	−38.00 ± 13.00	−0.037	−0.010	4/9/1
67976......	V499 Cen	−2.09 ± 1.99	9.23 ± 1.56	−23.91 ± 1.78	1.123 ± 0.078	−1.56 ± 0.28	323.00 ± 24.00	0.021	−0.002	3/9/3
68188......	ST CVn	0.00 ± 2.80	−14.17 ± 2.71	−14.31 ± 1.86	...	...	−85.00 ± 0.00	−0.020	−0.022	.../9/1
68292......	UY Boo	2.06 ± 1.92	2.32 ± 1.56	−46.73 ± 1.15	1.200 ± 0.122	−2.49 ± 0.16	144.00 ± 3.00	−0.003	−0.045	3/9/1
68908......	W CVn	1.15 ± 1.69	−19.30 ± 0.91	−15.63 ± 1.26	0.921 ± 0.053	−1.21 ± 0.14	18.00 ± 21.00	−0.017	−0.009	3/9/1
69759......	TV Boo	−0.50 ± 1.60	−5.80 ± 1.33	−34.93 ± 1.29	...	...	−85.00 ± 0.00	−0.008	−0.037	.../9/1
70079......	CW Lup	−20.09 ± 12.63	18.84 ± 12.89	−24.42 ± 13.15	...	...	...	...	...	.../.../...
70702......	ST Vir	−2.89 ± 3.22	−3.73 ± 3.72	−19.69 ± 2.90	1.365 ± 0.063	−0.88 ± 0.11	−22.00 ± 13.00	−0.001	−0.027	3/9/1
70751......	AF Vir	−6.81 ± 4.21	−58.14 ± 3.45	−0.71 ± 2.71	1.492 ± 0.099	−1.46 ± 0.37	−35.00 ± 14.00	−0.062	0.001	3/9/1
71186......	RS Boo	0.77 ± 1.57	6.56 ± 1.32	1.06 ± 1.13	0.779 ± 0.021	−0.32 ± 0.31	−9.00 ± 2.00	0.002	−0.012	3/9/1
72115......	TW Boo	−0.52 ± 1.77	−3.29 ± 1.50	−54.98 ± 1.64	1.280 ± 0.083	−1.41 ± 0.09	−99.00 ± 4.00	0.003	−0.059	3/9/1
72342......	AE Boo	1.38 ± 1.86	−25.63 ± 1.68	−38.34 ± 1.44	...	...	...	−0.023	−0.026	.../.../1
72444......	TY Aps	0.48 ± 2.47	−35.44 ± 1.75	8.18 ± 2.13	1.259 ± 0.073	−1.21 ± 0.11	100.00 ± 10.00	...	...	3/9/...
72691......	BT Dra	1.88 ± 1.60	2.35 ± 1.71	−32.09 ± 1.86	1.836 ± 0.128	−1.55 ± 0.07	−156.00 ± 30.00	0.001	−0.036	3/9/1
72721......	XZ Aps	0.71 ± 3.03	−17.67 ± 2.29	9.04 ± 2.99	1.617 ± 0.114	−1.57 ± 0.09	203.00 ± 24.00	...	...	3/9/...
74556......	AP Ser	−4.74 ± 2.30	−38.27 ± 2.63	−42.75 ± 1.98	...	...	−40.00 ± 0.00	−0.039	−0.044	.../9/1
75225......	TV CrB	−1.67 ± 3.49	−2.44 ± 3.40	−3.62 ± 3.59	1.659 ± 0.160	−2.33 ± 0.20	−157.00 ± 48.00	−0.003	−0.010	3/9/1
75942......	ST Boo	0.47 ± 1.75	−15.87 ± 1.32	−12.54 ± 1.47	1.197 ± 0.096	−1.86 ± 0.14	13.00 ± 4.00	−0.015	−0.017	3/9/1
75982......	VY Ser	−0.96 ± 1.68	−103.20 ± 1.92	−10.12 ± 1.40	0.802 ± 0.063	−1.82 ± 0.23	−145.00 ± 1.00	−0.098	−0.005	3/9/1
76172......	AR Ser	−3.73 ± 3.59	−39.61 ± 3.87	12.76 ± 2.99	1.747 ± 0.135	−1.78 ± 0.11	132.00 ± 4.00	−0.037	0.006	3/9/1
76313......	CG Lib	−5.76 ± 3.38	−61.15 ± 4.19	−25.49 ± 3.12	...	...	...	...	...	.../.../...
77663......	VY Lib	−0.46 ± 3.15	0.86 ± 3.43	−49.60 ± 2.66	1.316 ± 0.081	−1.32 ± 0.15	142.00 ± 10.00	−0.002	−0.065	3/9/1
77830......	AN Ser	−0.21 ± 2.48	−2.46 ± 3.29	−5.99 ± 2.25	0.961 ± 0.017	−0.04 ± 0.21	−47.00 ± 4.00	−0.003	−0.011	3/9/1
77997......	AT Ser	0.49 ± 2.99	−1.52 ± 3.46	−6.35 ± 3.52	1.489 ± 0.129	−2.05 ± 0.09	−58.00 ± 11.00	−0.001	−0.015	3/9/1
78417......	AR Her	1.24 ± 1.68	−61.70 ± 1.80	14.86 ± 2.18	1.250 ± 0.080	−1.40 ± 0.20	−349.00 ± 8.00	−0.065	0.012	4/9/1
78539......	LS Her	4.25 ± 2.01	−3.21 ± 1.98	6.04 ± 1.66	...	...	...	−0.002	0.001	.../.../1
78891......	BX Dra	3.38 ± 1.15	−7.80 ± 0.97	7.55 ± 1.07	1.687 ± 0.071	−0.75 ± 0.08	75.00 ± 30.00	−0.004	0.010	3/9/1
79974......	RV CrB	−0.26 ± 2.02	−22.25 ± 1.43	−27.43 ± 1.87	...	...	−100.00 ± 0.00	−0.021	−0.026	.../9/1
80102......	VZ Dra	1.73 ± 3.37	−7.36 ± 3.24	11.24 ± 3.66	...	...	...	−0.005	0.003	.../.../1
80402......	V445 Oph	0.08 ± 2.47	−11.35 ± 3.67	5.48 ± 2.36	0.786 ± 0.019	−0.23 ± 0.39	−22.00 ± 5.00	0.005	0.012	3/9/3
80853......	VX Her	0.47 ± 1.82	−54.20 ± 1.76	18.03 ± 1.57	0.917 ± 0.063	−1.52 ± 0.20	−377.00 ± 3.00	−0.047	0.017	4/9/1
80931......	VY Nor	9.89 ± 10.09	−30.68 ± 8.24	−38.68 ± 7.61	...	...	...	...	...	.../.../...
80990......	UV Oct	1.48 ± 0.94	−57.83 ± 0.89	−121.26 ± 0.94	0.525 ± 0.038	−1.61 ± 0.11	126.00 ± 12.00	−0.069	−0.123	3/9/3
81238......	RW Dra	1.80 ± 2.04	−11.75 ± 3.56	−5.08 ± 3.29	1.524 ± 0.098	−1.40 ± 0.11	−108.00 ± 22.00	−0.002	−0.008	3/9/1
83244......	RW TrA	1.34 ± 3.30	−9.11 ± 2.47	−5.89 ± 2.40	1.014 ± 0.014	0.07 ± 0.13	−39.00 ± 7.00	...	...	3/9/...
84233......	VZ Her	1.84 ± 1.77	−19.42 ± 1.53	−16.44 ± 1.68	1.306 ± 0.067	−1.03 ± 0.11	−115.00 ± 4.00	−0.024	−0.020	3/9/1
86512......	V494 Sco	10.54 ± 3.41	3.26 ± 4.05	−10.68 ± 2.35	0.746 ± 0.038	−1.01 ± 0.20	26.00 ± 30.00	−0.003	−0.006	4/9/3
87681......	TW Her	0.60 ± 1.64	3.10 ± 1.42	1.16 ± 1.43	1.116 ± 0.044	−0.67 ± 0.24	4.00 ± 16.00	−0.003	−0.007	3/9/1
87804......	WY Pav	1.10 ± 3.92	−31.26 ± 4.09	−27.57 ± 2.68	1.576 ± 0.079	−0.98 ± 0.37	−76.00 ± 14.00	...	...	3/9/...
87922......	V690 Sco	1.04 ± 3.22	−8.75 ± 3.78	−7.54 ± 1.51	...	...	−63.00 ± 0.00	...	...	.../9/...
88064......	S Ara	0.51 ± 2.15	−26.24 ± 2.29	−8.44 ± 1.24	0.856 ± 0.056	−1.43 ± 0.20	172.00 ± 13.00	−0.023	−0.015	4/9/3

TABLE 1—*Continued*

Star (HIC) (1)	Other Name (2)	π (mas) (3)	$\mu_{\alpha*}$ (mas yr^{-1}) (4)	μ_{δ} (mas yr^{-1}) (5)	D (kpc) (6)	[Fe/H] (dex) (7)	V_{rad} (km s^{-1}) (8)	$\mu_{\alpha*}^{old}$ (arcsec yr^{-1}) (9)	μ_{δ}^{old} (arcsec yr^{-1}) (10)	References[a] (DA/V/P) (11)
88402.......	MS Ara	10.00 ± 3.95	−2.88 ± 4.82	−37.39 ± 2.93	1.176 ± 0.079	−1.48 ± 0.11	101.00 ± 14.00	...	...	3/9/...
89326.......	V675 Sgr	4.30 ± 1.75	30.85 ± 2.09	−21.99 ± 1.18	0.853 ± 0.073	−2.01 ± 0.20	−105.00 ± 30.00	0.000	0.012	4/9/3
89450.......	V455 Oph	3.77 ± 4.18	−32.22 ± 3.29	−23.43 ± 3.13	1.667 ± 0.108	−1.42 ± 0.07	−36.00 ± 30.00	...	...	3/9/...
90053.......	IO Lyr	0.65 ± 2.36	−14.43 ± 2.45	30.08 ± 2.50	1.646 ± 0.113	−1.52 ± 0.11	−157.00 ± 30.00	−0.012	0.022	3/9/1
91634.......	CN Lyr	−2.68 ± 2.15	0.34 ± 1.61	−8.94 ± 1.95	0.979 ± 0.025	−0.26 ± 0.07	67.00 ± 30.00	−0.001	−0.016	3/9/1
92221.......	EZ Lyr	0.02 ± 6.37	−1.59 ± 5.92	13.10 ± 8.23	1.426 ± 0.100	−1.56 ± 0.20	−60.00 ± 23.00	−0.013	−0.002	4/9/3
92244.......	V413 CrA	0.66 ± 2.05	−35.10 ± 2.23	−25.57 ± 1.53	0.832 ± 0.048	−1.21 ± 0.16	−88.00 ± 10.00	...	...	3/9/...
93476.......	MT Tel	1.01 ± 1.26	−136.48 ± 1.38	−114.14 ± 0.91	...	...	72.00 ± 0.00	−0.137	−0.114	.../9/1
94134.......	XZ Dra	2.00 ± 0.97	11.89 ± 1.01	4.84 ± 1.19	0.686 ± 0.032	−0.87 ± 0.09	−30.00 ± 2.00	0.006	−0.007	3/9/1
94869.......	BK Dra	1.31 ± 1.36	−16.09 ± 1.05	29.97 ± 1.38	1.362 ± 0.121	−2.12 ± 0.21	−28.00 ± 30.00	...	...	3/9/...
95497.......	RR Lyr	4.38 ± 0.59	−109.59 ± 0.53	−195.54 ± 0.59	0.245 ± 0.016	−1.37 ± 0.08	−63.00 ± 8.00	−0.109	−0.194	3/9/3
95702.......	BN Vul	5.89 ± 2.11	−41.88 ± 1.67	−36.79 ± 1.94	0.658 ± 0.045	−1.52 ± 0.20	−267.00 ± 4.00	−0.048	−0.038	4/9/3
96101.......	V440 Sgr	−0.71 ± 2.10	−5.82 ± 2.01	−54.43 ± 1.11	0.705 ± 0.047	−1.47 ± 0.11	−62.00 ± 1.00	−0.002	−0.050	3/9/3
96112.......	XZ Cyg	2.28 ± 0.86	83.51 ± 1.00	−24.17 ± 0.92	0.565 ± 0.039	−1.52 ± 0.11	−119.00 ± 14.00	0.084	−0.022	3/9/3
96581.......	BN Pav	0.68 ± 5.00	0.80 ± 4.49	−4.50 ± 4.22	1.672 ± 0.103	−1.32 ± 0.15	114.00 ± 14.00	...	...	3/9/...
98265.......	BP Pav	−7.74 ± 4.02	−25.48 ± 3.19	−30.76 ± 3.23	1.847 ± 0.124	−1.48 ± 0.12	348.00 ± 14.00	...	...	3/9/...
99126.......	V2232 Sgr	10.00 ± 8.73	27.36 ± 8.29	−0.98 ± 7.70	...	...	...	...	...	.../.../...
101356......	V341 Aql	7.73 ± 5.82	34.86 ± 7.36	−25.02 ± 5.42	0.928 ± 0.059	−1.37 ± 0.11	−81.00 ± 4.00	0.035	−0.024	3/9/3
101453......	CH Aql	12.96 ± 9.36	19.07 ± 12.10	2.26 ± 9.03	...	...	...	0.002	0.011	.../.../1
101545......	IV Pav	2.54 ± 1.95	−8.00 ± 1.41	9.14 ± 1.90	...	...	...	...	...	.../.../...
102593......	DX Del	1.55 ± 1.54	14.75 ± 1.56	8.69 ± 0.97	0.563 ± 0.020	−0.56 ± 0.12	−45.00 ± 3.00	0.014	−0.012	3/9/1
103364......	UY Cyg	0.42 ± 2.06	−3.73 ± 1.43	−11.33 ± 1.56	1.042 ± 0.054	−1.03 ± 0.20	−2.00 ± 6.00	0.001	−0.008	4/9/3
103755......	RV Cap	−2.99 ± 2.46	18.77 ± 2.58	−106.21 ± 1.87	1.111 ± 0.084	−1.72 ± 0.28	−106.00 ± 7.00	0.024	−0.106	3/9/1
104613......	V Ind	1.50 ± 1.59	−71.47 ± 1.46	−83.42 ± 0.96	0.704 ± 0.048	−1.50 ± 0.11	202.00 ± 3.00	−0.070	−0.090	3/9/3
104930......	SW Aqr	1.15 ± 2.46	−42.05 ± 2.63	−58.87 ± 1.96	1.111 ± 0.065	−1.24 ± 0.11	−42.00 ± 8.00	−0.047	−0.061	3/9/1
105026......	Z Mic	−1.97 ± 3.17	16.51 ± 3.27	−7.58 ± 1.60	1.372 ± 0.083	−1.28 ± 0.20	−58.00 ± 10.00	...	...	3/9/...
105285......	YZ Cap	2.97 ± 2.52	−17.60 ± 3.26	−18.41 ± 1.47	...	...	−75.00 ± 0.00	−0.017	−0.011	.../9/1
106645......	SX Aqr	−0.53 ± 2.97	−39.84 ± 3.94	−47.04 ± 2.11	1.610 ± 0.127	−1.83 ± 0.25	−166.00 ± 7.00	−0.039	−0.051	3/9/1
106649......	RY Oct	5.77 ± 3.79	−3.83 ± 3.93	−29.41 ± 3.54	1.249 ± 0.099	−1.83 ± 0.11	37.00 ± 10.00	...	...	3/9/...
107078......	CG Peg	2.10 ± 2.06	−1.87 ± 2.04	−5.58 ± 1.52	1.021 ± 0.033	−0.48 ± 0.07	−4.00 ± 4.00	−0.001	−0.005	3/9/1
107935......	AV Peg	1.41 ± 1.72	13.37 ± 1.94	−7.65 ± 1.51	0.744 ± 0.016	−0.14 ± 0.22	−58.00 ± 1.00	0.014	−0.013	3/9/1
108057......	SS Oct	2.61 ± 2.79	3.33 ± 2.99	−34.73 ± 2.47	1.426 ± 0.102	−1.60 ± 0.11	312.00 ± 14.00	...	...	3/9/...
108839......	BV Aqr	3.74 ± 2.13	−0.25 ± 2.10	−21.13 ± 1.38	...	...	...	0.000	−0.006	.../.../1
109890......	DH Peg	0.15 ± 1.42	19.22 ± 2.03	−1.63 ± 0.98	...	...	−57.00 ± 0.00	0.035	−0.005	.../9/1
110213......	CZ Lac	−4.64 ± 15.72	26.83 ± 13.53	−5.09 ± 12.86	...	...	−120.00 ± 0.00	...	...	.../9/...
111839......	RZ Cep	0.22 ± 1.09	90.61 ± 1.38	189.10 ± 1.00	...	...	−1.00 ± 0.00	...	...	.../9/...
112532......	XZ Gru	0.55 ± 2.04	27.37 ± 1.75	−23.99 ± 1.37	...	...	...	...	...	.../.../...
112994......	BH Peg	−0.21 ± 1.82	−24.17 ± 1.60	−65.42 ± 1.39	0.824 ± 0.052	−1.38 ± 0.21	−278.00 ± 2.00	−0.020	−0.067	3/9/1
115135......	DN Aqr	4.20 ± 2.08	50.29 ± 2.68	−12.83 ± 1.64	1.293 ± 0.093	−1.63 ± 0.15	−214.00 ± 8.00	0.046	−0.016	3/9/3
115870......	RV Phe	2.48 ± 2.90	50.26 ± 2.52	−13.96 ± 1.80	1.645 ± 0.117	−1.60 ± 0.20	−99.00 ± 2.00	0.042	−0.019	4/9/3
116664......	BR Aqr	−4.01 ± 2.38	5.57 ± 2.42	−9.17 ± 1.68	1.304 ± 0.059	−0.84 ± 0.31	29.00 ± 10.00	0.005	0.000	3/9/1
116942......	VZ Peg	−1.61 ± 2.97	19.02 ± 2.46	−28.41 ± 1.85	...	...	...	0.019	−0.026	.../.../1
116958......	AT And	−2.70 ± 2.43	−7.05 ± 1.70	−50.29 ± 1.79	0.804 ± 0.040	−0.97 ± 0.20	−241.00 ± 11.00	−0.002	0.046	4/9/3

[a] See Table 2 for key to references.

TABLE 2

LITERATURE SOURCES

Source	Code
Distances/metal abundances ("DA"):	
Anthony-Twarog & Twarog 1994	1, 1s[a]
Bond 1980	2, 2s[a]
Layden 1994	3
Layden et al. 1996	4
Radial velocities ("V"):	
Bond 1980	1
Carney & Latham 1986	2
Norris, Bessell, & Pickles 1985	3
Barbier-Brossat 1989	4
Wilson 1953	5
Evans 1978	6
Griffin et al. 1982	7
Papers quoted by Bond 1980	8
Layden 1994	9
Previous results of proper motions ("P"):	
Lick Northern Proper Motion Catalogue	1
Hipparcos Input Catalogue	2
Wan, Mao, & Ji 1980	3

[a] Spectroscopic abundances compiled by Anthony-Twarog & Twarog 1994.

Input Catalogue (ESA 1992). Values not included in that list are taken from the recently completed catalog of the Lick Northern Proper Motion Program, the NPM1 Catalog (Klemola, Hanson, & Jones 1993), in which the measurements are accurate to ~ 5 mas yr^{-1} on average.

To assess the quality of the *Hipparcos* data, we show in Figure 2 the difference between previous and *Hipparcos* measurements for proper-motion components. While the previous measurements of $\mu_{\alpha *}$ and μ_δ for stars having large proper motions are compatible with the *Hipparcos* measurements, we see a large, systematic difference between the previous and the *Hipparcos* measurements for stars with small proper motions. This suggests that the new, higher accuracy *Hipparcos* measurements will provide insight into the kinematics of stars with small proper motions. We note that these stars, including those with noneccentric orbits, are of particular importance to understanding the formation process of the Galaxy.

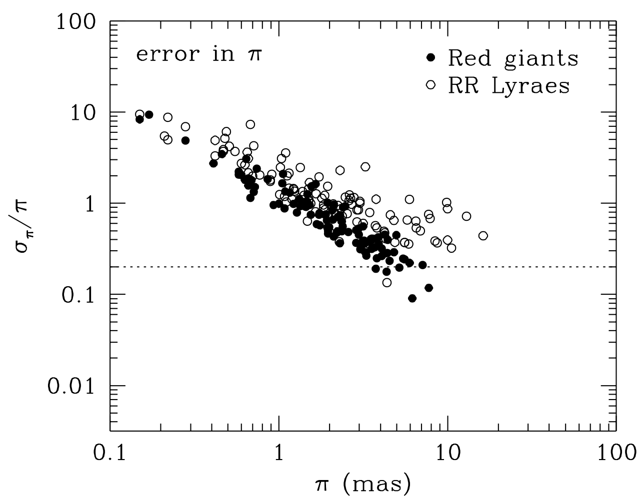

FIG. 1.—Distribution of relative parallax errors σ_π/π. Filled and open circles denote red giants and RR Lyrae stars, respectively.

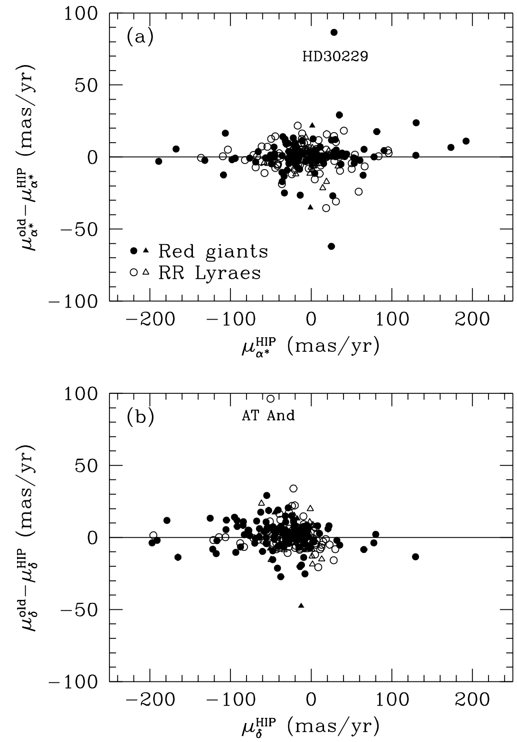

FIG. 2.—Difference between the previous ("old") and *Hipparcos* ("HIP") measurements for proper motions (*a*) $\mu_{\alpha *}$ and (*b*) μ_δ. Filled and open circles denote red giants and RR Lyrae stars, respectively, with small relative errors in proper motions ($|\mu_{\alpha *}| > \sigma_{\mu_{\alpha *}}$ and $|\mu_\delta| > \sigma_{\mu_\delta}$), while filled and open triangles are for large errors ($|\mu_{\alpha *}| \le \sigma_{\mu_{\alpha *}}$ and $|\mu_\delta| \le \sigma_{\mu_\delta}$).

2.3. *Distances and Abundances*

2.3.1. *Red Giants*

The absolute V magnitudes M_V, photometric distances D, and metal abundances [Fe/H] of our red giants have been derived by Bond (1980) based on Strömgren *uvby* photometry. Corrections for Galactic reddening were estimated from a simple csc $|b|$ model, where b is the Galactic latitude of the star. Some stars from the original Bond sample have been reanalyzed by Carney & Latham (1986) using the same procedure, and by NBP using DDO photometry. Recently, Anthony-Twarog & Twarog (1994, hereafter ATT) updated the values of D and [Fe/H] for most of the stars in Bond's sample. They obtained new *uvby* photometry with CCDs and estimated the realistic reddening effects on red giants by using the maps of Burstein & Heiles (1982). The revised photometric metal abundances appear to be in excellent agreement with those from high-dispersion spectroscopy. It was also pointed out that the metallicity calibration of the DDO photometry of NBP and MFF provides reliable [Fe/H] estimates only near -0.8 and -2.3, systematically underestimating the metallicity by about 0.5 dex at $[\mathrm{Fe/H}]_{\mathrm{DDO}} \sim -1.2$ (Twarog & Anthony-Twarog 1994, 1996; Ryan & Lambert 1995). This point raises the important issue of the existence of metal-poor stars with disklike kinematics, discussed in § 3.2.

For our red giants, we adopt ATT's estimates of D and [Fe/H], except for four stars (HIC 5458, 38621, 65852, 71087) that they did not analyze. We adopt Bond's (1980) estimates for such stars. A standard error in [Fe/H] is taken to be 0.16 dex, which is a typical difference between the photometric and the spectroscopic abundances in the ATT sample. For some of our red giants, we use the spectroscopic abundances and associated errors that have been determined by previous workers and compiled by ATT. A standard relative error in the derived distances is taken to be 0.08. This is because the ATT calibration of M_V is based on the relation of color $B-V$ to absolute magnitude M_V in the work of NBP, where M_V has a typical error of 0.4 mag.

We next compare the photometric distances with those derived from the *Hipparcos* parallaxes, using five red giants (HIC 5445, 5458, 29992, 68594, 92167) for which the errors in *Hipparcos* parallaxes are relatively small ($|\sigma_\pi/\pi| \leq 0.2$). The mean difference between these distances is found to be only 15 pc, with a dispersion of 55 pc, yielding a 25%–26% relative error in the distances. This level of uncertainty may be acceptable if a typical error of 8% in their photometric distances is also taken into account. On the contrary, we necessarily use the photometric distances for the stars with larger parallax errors because we see no correlation between their photometric and parallactic distances.

2.3.2. *RR Lyrae Stars*

The metal abundances [Fe/H] of our RR Lyrae stars are taken from the work of Layden (1994). These values have been measured from the strength of the Ca II K line relative to the Balmer lines after calibrating it to the [Fe/H] abundance scale for the globular clusters studied by Zinn & West (1984). A typical error in [Fe/H] is 0.15–0.2 dex. For some of our RR Lyrae stars that were not observed by Layden (1994), we adopt the [Fe/H] values that were estimated by Layden et al. (1996) using the published ΔS values. The intensity-mean apparent V magnitude and interstellar reddenings are taken from the work of Layden et al. (1996) based on the photometry of Clube & Dawe (1980) and the reddening maps of Burstein & Heiles (1982), Blanco (1992), and FitzGerald (1968, 1987).

To determine the photometric distances D to our RR Lyrae stars, we calibrate their absolute M_V magnitudes with [Fe/H] by assuming a linear relation $M_V = a[\mathrm{Fe/H}] + b$, where the slope a and the intercept b are both constants. There have been many approaches to determining a and b, including Baade-Wesselink analyses, main-sequence fitting of globular clusters, and the statistical parallax method (for details, see, e.g., Carney, Storm, & Jones 1992; Layden et al. 1996). It can be seen from Figure 7 of Layden et al. (1996) that various M_V-[Fe/H] relations lie between the relation of Carney et al. (1992; $a = 0.15$, $b = 1.01$), yielding the faintest M_V, and that of Sandage (1993; $a = 0.30$, $b = 0.94$), yielding the brightest M_V. The typical magnitude difference between these two extrema changes from $\Delta M_V \approx 0.15$ to $M_V \approx 0.37$ mag when [Fe/H] decreases from -0.5 to -2.0 dex. We simply take a mean of these extreme M_V values because the present analysis is not very sensitive to which M_V-[Fe/H] relation is adopted. The difference between this mean and either of the two extreme M_V values, which dominates the error that originates from the measurement error in [Fe/H], is used as a standard error in M_V.

We note that the errors in M_V are the main source of uncertainties in estimates of photometric distances. The relative errors of these distances turn out to be less than 10% and are more accurate even than those derived from the *Hipparcos* parallaxes (see Fig. 1). Therefore, we use the photometric distances for our RR Lyrae stars, except for HIC 95497, which was observed most accurately with *Hipparcos*. The small parallax error $|\sigma_\pi/\pi| \leq 0.14$ of this star amounts to only a 6.9%–7.5% relative error in the distance. Similar to red giants, other RR Lyrae stars with much larger parallax errors show no correlation between their photometric and parallactic distances.

The distributions of distances and metal abundances of our program stars are shown in Figures 3*a* and 3*b*, respectively, where the hatched histograms are for red giants and the solid histograms are for RR Lyrae stars. It is apparent that the stars are sampled mostly within ~ 2 kpc of the Sun. The metal abundances of red giants are less than $[\mathrm{Fe/H}] = -1$, with a mean of -1.8, whereas those for RR Lyrae stars are peaked at $[\mathrm{Fe/H}] \sim -1.5$, showing a long tail on both sides of the peak metallicity. It should be noted that metal abundances of red giants extend above the limit $[\mathrm{Fe/H}] = -1.5$ in the original analysis of Bond (1980), as a result of our use of the revised metallicity calibration by ATT.

The metallicity distribution for a much larger sample of field halo stars was derived by Laird et al. (1988) and Ryan & Norris (1991), which involves a small contribution from both old thin disk and thick-disk stars with $[\mathrm{Fe/H}] > -1$ (Fig. 3*b*, *solid curve*). Such a distribution is not dissimilar to that for our whole sample of red giant and RR Lyrae stars. It is therefore suggested that in the metallicity range [Fe/

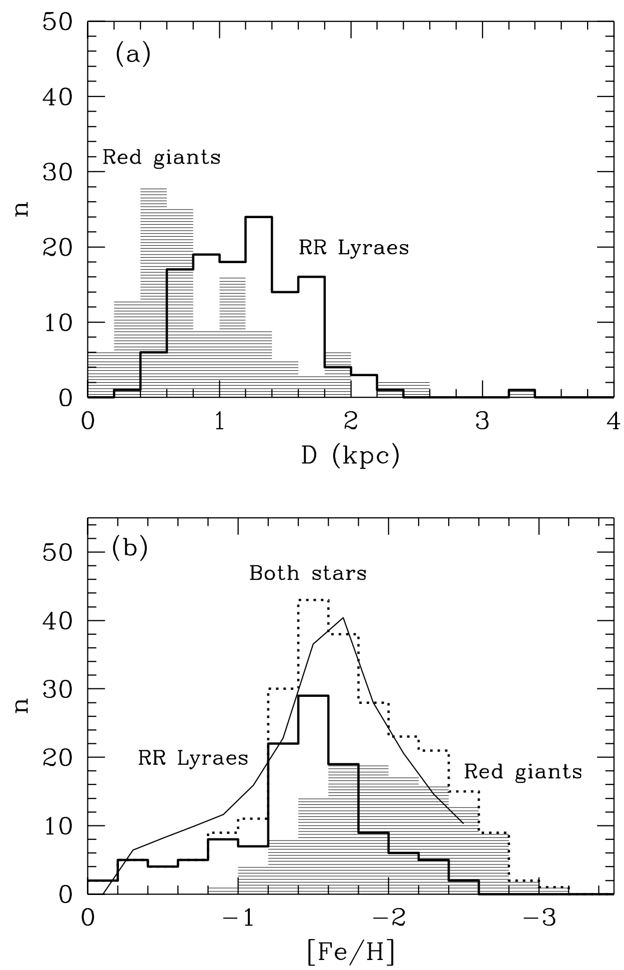

FIG. 3.—Distributions of (*a*) distances and (*b*) metallicities for red giants (*hatched histograms*) and RR Lyrae stars (*solid histograms*). In (*b*), the dotted histogram is for both stars, while the solid curve shows the likely true metallicity distribution of halo stars derived by Laird et al. (1988).

TABLE 3

MEAN VELOCITIES AND VELOCITY DISPERSIONS OF THE SAMPLE STARS

[Fe/H] (dex)	N	$\langle U \rangle$	$\langle V \rangle$	$\langle W \rangle$	σ_U	σ_V	σ_W
0.1 to −0.4......	4	14 ± 7	−21 ± 8	9 ± 9	40 ± 16	23 ± 10	31 ± 13
−0.4 to −1.0......	13	31 ± 11	−78 ± 15	−11 ± 17	84 ± 17	86 ± 18	64 ± 13
−1.0 to −1.6......	69	−32 ± 15	−187 ± 16	0 ± 13	154 ± 13	100 ± 9	94 ± 8
≤ −1.6	124	16 ± 18	−217 ± 21	−10 ± 12	161 ± 10	115 ± 7	108 ± 7
≤ −1.8	93	7 ± 18	−216 ± 22	−14 ± 11	160 ± 12	119 ± 9	108 ± 8
≤ −2.0	64	−1 ± 19	−217 ± 24	−20 ± 11	159 ± 14	117 ± 10	111 ± 10

NOTE.—Velocities and dispersions in km s^{-1}.

H] < −1 possible incompleteness in our sample may not affect the following analysis.[2]

2.4. *Radial Velocities*

A number of previous workers have measured radial velocities $V_{\rm rad}$ for our red giants, with different accuracies. These include Bond (1980), NBP, Carney & Latham (1986), Barbier-Brossat (1989), and others, as listed in Table 2. If only one work reported $V_{\rm rad}$ for a certain star, we simply used it together with the published value of $\sigma_{V_{\rm rad}}$, or with $\sigma_{V_{\rm rad}} = 5$ km s^{-1} if not given. If more than one work reports values of $V_{\rm rad}$ for a certain star, we adopt the value of $V_{\rm rad}$ that has the smallest $\sigma_{V_{\rm rad}}$ if given. Otherwise we take the mean of the $V_{\rm rad}$'s and estimate $\sigma_{V_{\rm rad}}$ from the standard dispersion from the mean. In the latter case, more than one code number is listed in column (11) of Table 1. For our RR Lyrae stars, however, the primary source of $V_{\rm rad}$ and $\sigma_{V_{\rm rad}}$ is the work of Layden (1994).

3. KINEMATICS

3.1. *Individual and Systematic Motions*

Given a set of distance, proper-motion, and radial velocity data for each star, we derive its three-dimensional spatial velocity components U, V, and W directed to the Galactic anticenter, the rotation, and the north pole, respectively. These velocity components are corrected for the local solar motion $(U_\odot, V_\odot, W_\odot) = (-9, 12, 7)$ km s^{-1} with respect to the local standard of rest (Mihalas & Binney 1981). Associated errors in (U, V, W) are calculated by using the formulation of Johnson & Soderblom (1987). We also derive the velocity components (V_R, V_ϕ) and their errors in the cylindrical rest frame (R, ϕ), under the assumptions that the solar distance from the Galactic center is $R_\odot = 8.5$ kpc and that the rotational speed of the LSR is $V_{\rm LSR} = 220$ km s^{-1}.

Figure 4 shows the U, V, and W velocities of the individual stars as a function of [Fe/H]. We note that our RR Lyrae sample largely overlaps with Layden's (1995) and that the velocity distribution shown here looks similar to that displayed in his paper. This suggests that the kinematics of RR Lyrae stars based on previous proper-motion surveys (NPM1; Wan, Mao, & Ji 1980) may remain unchanged even when using the *Hipparcos* proper motions.

[2] This statement is valid only if there is no age difference between the halo and thick disk, which affects the RR Lyrae contributions in a metallicity range relevant to the thick disk. In this respect, in the latter part of this paper, we obtain almost the same contribution of red giant and RR Lyrae stars to the metal-weak thick disk at −1.6 < [Fe/H] ≤ −1 (see Table 5 below). This may support the absence of a significant age difference, at least for [Fe/H] < −1.

It is evident from this figure that metal-poor stars with [Fe/H] < −1 have large random motions compared with stars with [Fe/H] > −1, thus indicating that the kinematic properties change rather abruptly at [Fe/H] ∼ −1.2 to −1, as claimed by Yoshii & Saio (1979) and subsequently confirmed by MFF from their sample of red giants and by Layden (1995) from his sample of RR Lyrae stars. This may suggest that the formation of disk component with [Fe/H] > −1 was distinct from that of the more metal-poor halo component.

Table 3 shows the mean velocities ($\langle U \rangle$, $\langle V \rangle$, $\langle W \rangle$) and velocity dispersions (σ_U, σ_V, σ_W) of stars in several metallicity ranges. The velocity dispersion is estimated from the standard deviation from the mean after correction for the observational errors. It is evident that more metal-poor stars are characterized by larger $|\langle V \rangle|$, that is, larger rota-

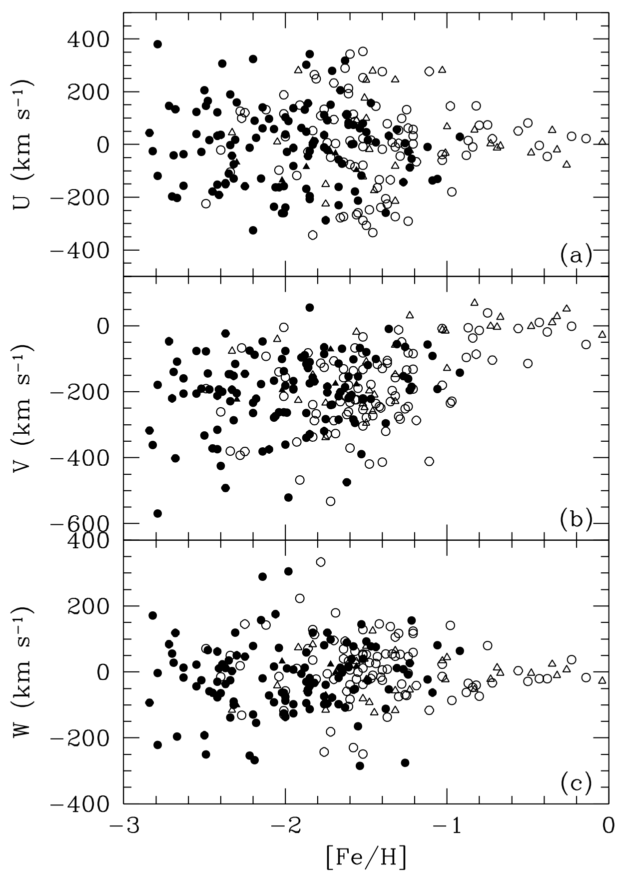

FIG. 4.—(U, V, W) velocity components vs. [Fe/H] for the sample. Symbols are the same as in Fig. 2.

tional lag behind the LSR, and larger velocity dispersions. In particular, metal-poor stars with [Fe/H] ≤ -1.6, which may well represent the halo component, have no net rotation ($V_{\rm LSR} - |\langle V \rangle| \approx 3 \pm 21$ km s^{-1}) and no systematic motions in other velocity components within the range of the errors ($\langle U \rangle = 16 \pm 18$ km s^{-1}, $\langle W \rangle = -10 \pm 12$ km s^{-1}). The velocity ellipsoid for these stars is radially elongated, $(\sigma_U, \sigma_V, \sigma_W) = (161 \pm 10, 115 \pm 7, 108 \pm 7)$ km s^{-1}, in reasonable agreement with previous results (e.g., Beers & Sommer-Larsen 1995). The shape of the velocity ellipsoid appears unchanged even if we adopt a more restricted metallicity criterion of either [Fe/H] ≤ -1.8 or [Fe/H] ≤ -2 for selecting the halo stars. We note that the V_R and V_ϕ velocity components in the cylindrical rest frame are essentially the same as U and $V_{\rm LSR} + V$, respectively, because our program stars are localized in the solar neighborhood (Fig. 3*a*).

To examine more closely the rotational properties, we plot $\langle V_\phi \rangle$, σ_ϕ, and $\langle V_\phi \rangle / \sigma_\phi$ against [Fe/H] in Figure 5; their values are tabulated in Table 4. Here the ratio $\langle V_\phi \rangle / \sigma_\phi$ measures how much the system is rotationally supported. It is clearly seen that the rotational properties change rather discontinuously at [Fe/H] ~ -1.4 to -1. For [Fe/H] > -1, there is an indication that $\langle V_\phi \rangle$ correlates with [Fe/H], although the small number of these metal-rich stars ($N = 17$) makes its significance less definite. On the other hand, for [Fe/H] < -1.4 there is no obvious variation in $\langle V_\phi \rangle$ and $\langle V_\phi \rangle / \sigma_\phi$ with decreasing [Fe/H], and $\langle V_\phi \rangle$ is consistent with zero rotation within 1 σ errors. This result confirms earlier conclusions (Norris 1986; Carney 1988; Zinn 1988; Norris & Ryan 1989) that invalidate the Sandage & Fouts (1987) result of a linear dependence of $\langle V_\phi \rangle$ on [Fe/H]. Thus the ELS hypothesis of a monolithic free-fall collapse from halo to disk is not supported (see Norris & Ryan 1989 for detailed discussion). It is interesting to note that the stars with $-1.4 \leq$ [Fe/H] ≤ -1 have a slightly larger $\langle V_\phi \rangle$ than the more metal-poor stars, as also realized by Layden (1995) from his sample of RR Lyrae stars. In the next subsection, we will investigate in more detail whether this suggests an intermediate component between halo and thick disk, or, more specifically, whether this manifests a metal-weak tail of the thick disk component.

3.2. *Is There a Metal-weak Thick Disk?*

MFF suggested from their sample of red giants that there is a significant number of stars with disklike kinematics but low metallicity, in the range $-1.6 \leq$ [Fe/H] ≤ -1, near the Galactic plane ($|z| < 1$ kpc). They found that this

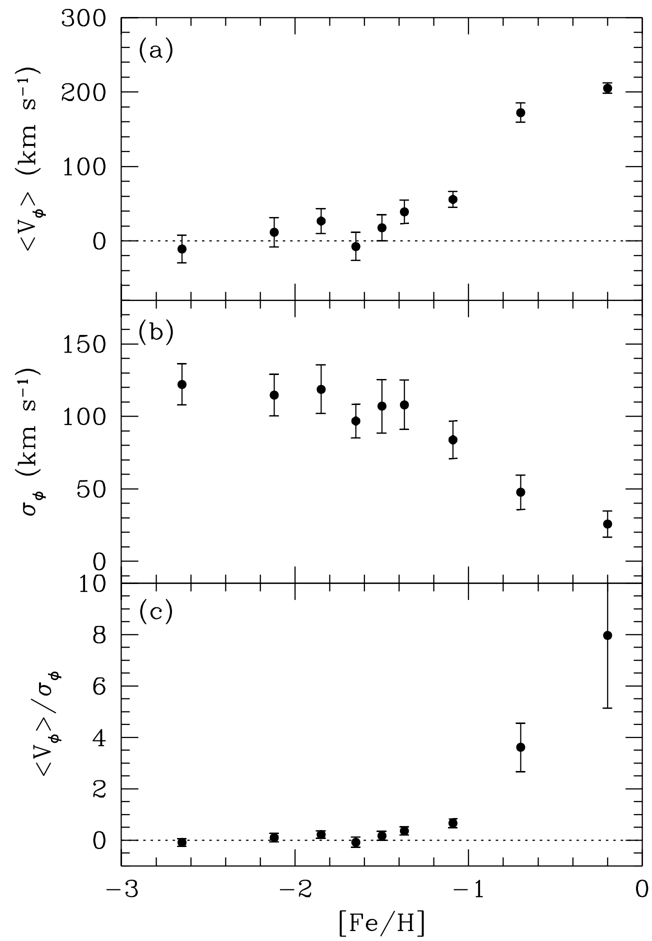

FIG. 5.—Rotational properties vs. [Fe/H] for the sample. (*a*) Mean rotation $\langle V_\phi \rangle$; (*b*) velocity dispersion in the ϕ-direction, σ_ϕ; (*c*) the ratio $\langle V_\phi \rangle / \sigma_\phi$.

"metal-weak thick disk" (MWTD) rotates rapidly, at $V \approx 170$ km s^{-1}, accounting for about 72% of the stars in this metallicity range, whereas they found no evidence of the MWTD for RR Lyrae stars. Rodgers & Roberts (1993) also argued for the MWTD from their finding of a large number of candidate blue horizontal-branch (BHB) stars with disklike kinematics (but see Wilhelm 1995 for different results using BHB stars, as discussed in Layden 1995). However, Layden (1995) found that a modest fraction of his sample of RR Lyrae stars show disklike kinematics only in the metallicity range $-1.3 \leq$ [Fe/H] ≤ -1. Beers & Sommer-Larsen (1995) argued that the MWTD component was

TABLE 4

ROTATIONAL PROPERTIES OF THE SAMPLE STARS

[Fe/H] (dex)	⟨[Fe/H]⟩ (dex)	N	$\langle V_\phi \rangle$ (km s^{-1})	σ_ϕ (km s^{-1})	$\langle V_\phi \rangle / \sigma_\phi$
0.10 to −0.50......	−0.20	5	205 ± 7	26 ± 9	7.97 ± 2.83
−0.50 to −0.90......	−0.70	9	172 ± 13	48 ± 12	3.61 ± 0.94
−0.90 to −1.28......	−1.09	22	56 ± 11	84 ± 13	0.66 ± 0.17
−1.28 to −1.45......	−1.37	21	39 ± 16	108 ± 17	0.36 ± 0.16
−1.45 to −1.56......	−1.50	18	18 ± 17	107 ± 18	0.17 ± 0.17
−1.56 to −1.75......	−1.65	36	−7 ± 19	97 ± 12	−0.08 ± 0.20
−1.75 to −1.95......	−1.85	26	27 ± 17	119 ± 17	0.22 ± 0.14
−1.95 to −2.30......	−2.12	33	12 ± 20	115 ± 14	0.10 ± 0.17
−2.30 to −3.01......	−2.65	38	−11 ± 19	122 ± 14	−0.09 ± 0.15

confirmed from their large sample of metal-poor stars. Their MWTD, rotating at $V \approx 195$ km s^{-1}, accounts for about 60% of the stars in the range $-1.6 \leq$ [Fe/H] ≤ -1 in the solar neighborhood, and it possesses an extremely metal-weak tail down to [Fe/H] ≤ -2. However, because of the heterogeneous nature of their sample, which includes various types of stars in different evolutionary phases, it is not obvious whether all types of stars or only subsamples like red giants constitute a large fraction in the MWTD component. On the other hand, ATT demonstrated that the metal abundances of red giants in the range $-1.6 \leq$ [Fe/H] ≤ -1 had been underestimated by at most 0.5 dex in the DDO photometry of NBP and MFF. Thus, many of the stars that were previously assigned to the MWTD belong to the more metal-rich old disk and/or thick disk with [Fe/H] > -1. This suggests that the evidence claimed for the MWTD component may be less significant than previously thought (see also the further discussion in Ryan & Lambert 1995; Twarog & Anthony-Twarog 1996).

In view of these controversies, we examine whether our sample of metal-poor stars, especially red giants having updated metal abundances and kinematics, supports the existence of the MWTD component. Following the procedure adopted by MFF and subsequent workers, we divide our sample into stars at $|z| < 1$ kpc and at $|z| \geq 1$ kpc; we show the frequency distribution of V_ϕ for four metallicity intervals in Figure 6. At $|z| < 1$ kpc, the metal-rich stars with [Fe/H] ≥ -1 (Figs. 6*a*, 6*b*) are characterized by a high rotational velocity, $V_\phi = 200$–220 km s^{-1}. Because of the small number of such stars, it is not clear whether the V_ϕ velocity distribution has a Gaussian nature as MFF reported. For the stars of our concern in the metallicity range $-1.6 \leq$ [Fe/H] ≤ -1 (Fig. 6*c*), we are unable to verify MFF's finding of a strongly asymmetric V_ϕ-distribution

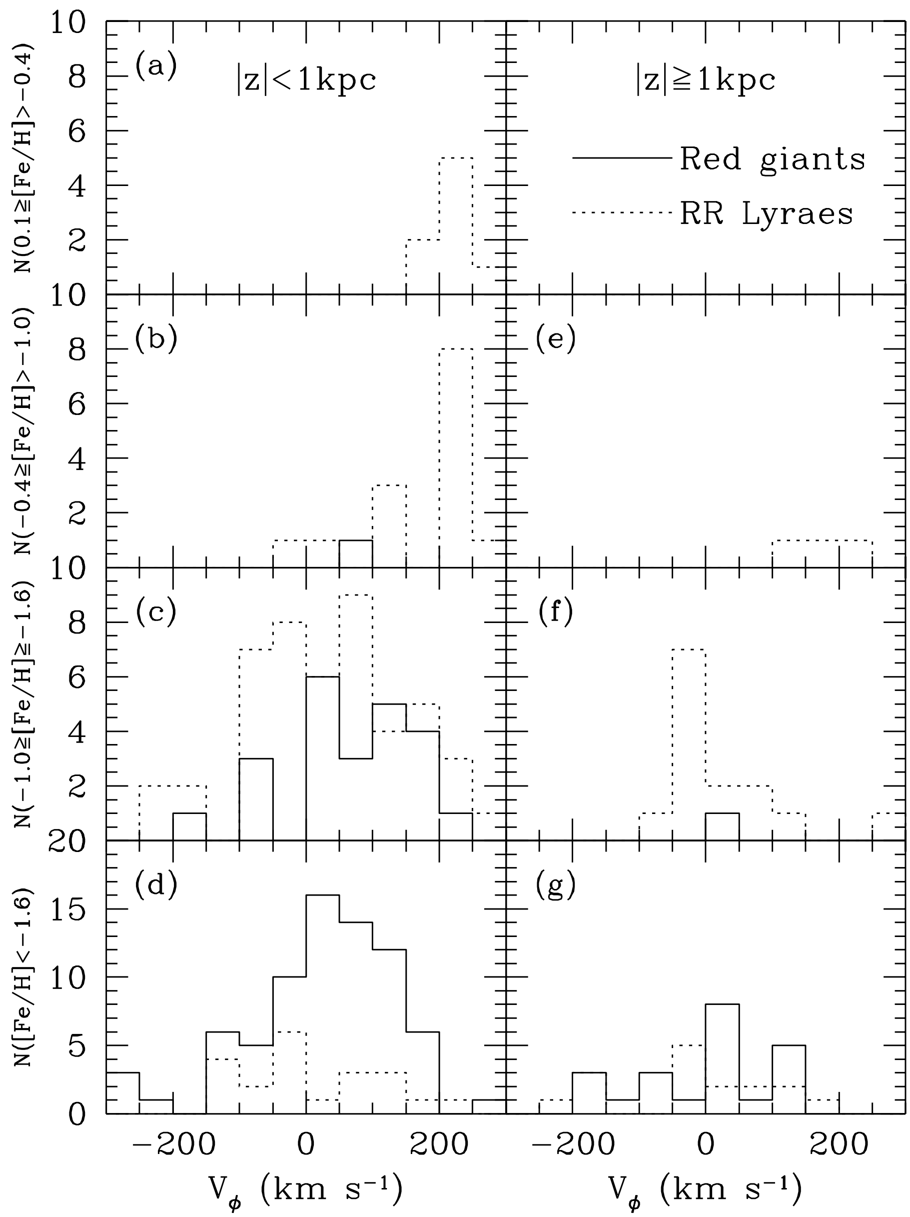

FIG. 6.—Distributions of V_ϕ in different metallicity ranges for red giants (*solid histograms*) and RR Lyrae stars (*dotted histograms*). The left and right columns are for $|z| < 1$ kpc and $|z| \geq 1$ kpc, respectively, and the metallicity ranges are indicated in the labels for the vertical axes. Note that in the range $-1.6 \leq$ [Fe/H] ≤ -1 (*c*), the deviation from a single Gaussian is less significant than previously reported.

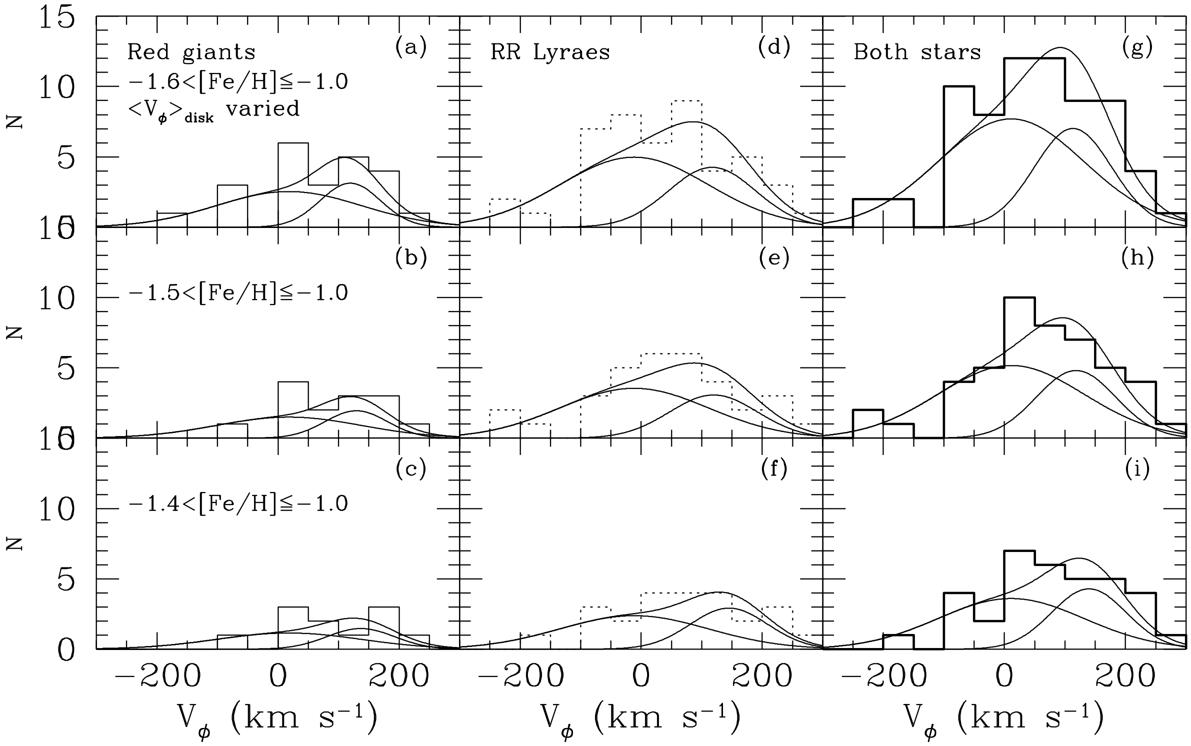

FIG. 7.—Results of the maximum likelihood method for reproducing the V_ϕ-distribution at $|z| < 1$ kpc, based on a mixture of two Gaussian components (halo plus disk). The mean rotation of the disk $\langle V_\phi \rangle_{\rm disk}$ is one of the variable parameters in the fitting. The metallicity ranges are (*a, d, g*) $-1.6 <$ [Fe/H] ≤ -1; (*b, e, h*) $-1.5 <$ [Fe/H] ≤ -1; and (*c, f, i*) $-1.4 <$ [Fe/H] ≤ -1.

(their Fig. 7*c*), which they considered to be evidence for the MWTD component. There is indeed an indication that the V_ϕ-distribution for our red giants is somewhat skewed toward positive V_ϕ, but it is not as significant in demonstrating the MWTD component. Furthermore, the V_ϕ-distribution for our red giants is similar to those derived by MFF and Layden (1995) from their samples of RR Lyrae stars, where a possible contribution of the MWTD was already shown to be modest in such a metallicity range. For the more metal-poor stars with [Fe/H] ≤ -1.6 (Fig. 6*d*), the V_ϕ-distribution for the composite sample of red giant and RR Lyrae stars is essentially the same as that presented in MFF, and this is also the case for stars at $|z| \geq 1$ kpc (Figs. 6*f*, 6*g*).

TABLE 5

PARAMETERS OF THE METAL-WEAK THICK DISK AT $|z| < 1$ kpc

Stars	N	$\langle V_\phi \rangle_{\rm disk}$ (km s^{-1})	$\sigma_{\phi,\rm disk}$ (km s^{-1})	F
$\langle V_\phi \rangle_{\rm disk}$ Variable				
[Fe/H] = −1.0 to −1.6 dex:				
Red giant	23	120	50	0.34
RR Lyrae...........	46	117	72	0.33
Both	69	113	64	0.33
[Fe/H] = −1.0 to −1.5 dex:				
Red giant	14	129	51	0.36
RR Lyrae...........	33	120	73	0.34
Both	47	118	66	0.34
[Fe/H] = −1.0 to −1.4 dex:				
Red giant	11	137	56	0.37
RR Lyrae...........	24	145	64	0.39
Both	35	140	62	0.38
$\langle V_\phi \rangle_{\rm disk}$ Fixed at 195 km s^{-1}				
[Fe/H] = −1.0 to −1.6 dex:				
Red giant	23	195	44	0.09
RR Lyrae...........	46	195	33	0.12
Both	69	195	36	0.09
[Fe/H] = −1.0 to −1.5 dex:				
Red giant	14	195	41	0.18
RR Lyrae...........	33	195	50	0.15
Both	47	195	41	0.12
[Fe/H] = −1.0 to −1.4 dex:				
Red giant	11	195	34	0.26
RR Lyrae...........	24	195	54	0.28
Both	35	195	41	0.23

To examine more quantitatively the existence of the MWTD component in the stars with $-1.6 \leq$ [Fe/H] ≤ -1 (Fig. 6*c*), we fitted the data to a mixture of two Gaussian distributions, representing the separate components of halo and disk. Under the assumption that the mean velocity $\langle V_\phi \rangle_{\rm halo}$ and velocity dispersion $\sigma_{\phi,\rm halo}$ for the halo are fixed at the values for the stars with [Fe/H] < -1.6 in Figure 6*d*, we evaluate the best-fit values of the disk quantities such as $\langle V_\phi \rangle_{\rm disk}$ and $\sigma_{\phi,\rm disk}$, as well as the disk fraction F. The likelihood function for stars with V_ϕ^i is then given by

$$\log f(F, \langle V_\phi \rangle_{\rm disk}, \sigma_{\phi,\rm disk}) = \sum_i \log [F f^i_{\rm disk} + (1 - F) f^i_{\rm halo}] \quad (1)$$

(MFF), where

$$f^i_{\rm disk} = \frac{1}{\sigma_{\phi,\rm disk}\sqrt{2\pi}} \exp\left[-\frac{(V_\phi^i - \langle V_\phi \rangle_{\rm disk})^2}{2\sigma^2_{\phi,\rm disk}}\right], \quad (2)$$

$$f^i_{\rm halo} = \frac{1}{\sigma_{\phi,\rm halo}\sqrt{2\pi}} \exp\left[-\frac{(V_\phi^i - \langle V_\phi \rangle_{\rm halo})^2}{2\sigma^2_{\phi,\rm halo}}\right]. \quad (3)$$

Before applying the maximum likelihood analysis, we determine the halo quantities $\langle V_\phi \rangle_{\rm halo}$ and $\sigma_{\phi,\rm halo}$ for each of the samples with [Fe/H] < -1.6 consisting of red giant and RR Lyrae stars. Fixing these halo quantities, we then find the best-fit values of the disk quantities in three low-metallicity ranges, $-1.6 <$ [Fe/H] ≤ -1, $-1.5 <$ [Fe/H] ≤ -1, and $-1.4 <$ [Fe/H] ≤ -1. Figure 7 shows histograms of the V_ϕ velocity distribution in these low-metallicity ranges for red giants (*left*), RR Lyrae stars (*middle*), and both groups (*right*). The results of the maximum likelihood analysis are shown by curves in Figure 7 and are tabulated in Table 5. In sharp contrast to the results of MFF and Beers & Sommer-Larsen (1995), we find only a modest disk fraction of $F \sim 0.3$ for either red giants, RR Lyrae stars, or both. It is also interesting to note that the derived mean velocity, $\langle V_\phi \rangle_{\rm disk} \approx 118$ km s^{-1}, is much smaller than previously reported.

We now attempt to determine the fraction of the more rapidly rotating disk at $\langle V_\phi \rangle_{\rm disk} \approx 195$ km s^{-1} that was postulated as the MWTD by Beers & Sommer-Larsen (1995). For this purpose, we further fix $\langle V_\phi \rangle_{\rm disk} = 195$ km s^{-1} and find the best-fit values of $\sigma_{\phi,\rm disk}$ and F. The results in Table 5 indicate that the fraction of this rapidly rotating disk is only 0.1–0.2, and therefore its existence is quite marginal. Given such a small fraction of the rapidly rotating disk, however, the present analysis alone cannot tell which type of MWTD, rotating slowly at $\langle V_\phi \rangle_{\rm disk} \sim 120$ km s^{-1} or rapidly at $\langle V_\phi \rangle_{\rm disk} \sim 200$ km s^{-1}, is actually preferred. We will return to this problem in § 4.4, analyzing the orbital motions of stars.

4. ORBITAL PROPERTIES

Stars observed in the solar neighborhood have traveled from different, often very distant, locations within the Galaxy. In this section, we investigate the orbital motions of our program stars in a model gravitational potential of the Galaxy. We will especially focus on the distribution of orbital eccentricity and use it as diagnostic for studying the global dynamics of the Galaxy.

4.1. *Gravitational Potential*

We investigate the space motions of our program stars in two representative types of the gravitational potential that are both axisymmetric and stationary. One is the two-dimensional potential $\Phi(R)_{\rm ELS}$ adopted first by ELS and subsequently by most workers. Although this potential provides the projected orbits onto the Galactic plane, we can compare the planar orbits of our program stars directly with those previously reported. Another is the more realistic three-dimensional potential that allows vertical motion above and below the Galactic plane. Sommer-Larsen & Zhen (1990, hereafter SLZ) adjusted the parameters in the analytic Stäckel potential and reproduced the mass model of Bahcall, Schmidt, & Soneira (1982). We adopt this potential, $\Phi(R, z)_{\rm SLZ}$, because the analytic potential has the great advantage of maintaining clarity in the analysis.

Some cautions are in order regarding the use of $\Phi(R)_{\rm ELS}$. The motivation behind this potential is to reproduce the mass distribution in the disk without including a massive dark halo. Thus, some stars with large velocities or in highly eccentric orbits become unbound in the original ELS potential. In order to effectively take into account the effects of a massive halo, we derive the escape velocity $V_{\rm esc}$ from our sample stars and place a new constraint on $\Phi(R)_{\rm ELS}$.

Three of our red giants were found to possess a rest-frame velocity in excess of 400 km s^{-1}: HIC 69470 (437 km s^{-1}), HIC 75263 (454 km s^{-1}), and HIC 104191 (562 km s^{-1}). For the extremely high velocity star HIC 104191 (HD 200654), however, there is a large discrepancy among the estimates of D and [Fe/H] by ATT, NBP, and Bond (1980). Instead of the value obtained using ATT's (D, [Fe/H]) = (0.463 kpc, -2.79), the estimates by NBP (0.404 kpc, -2.26) and Bond (1980) (0.320 kpc, -2.40) yield rest-frame velocities of 472 and 348 km s^{-1}, respectively. Since the reason for such a large discrepancy is not known, we exclude HIC 104191 and adopt $V_{\rm esc} = 450$ km s^{-1}, in agreement with the result of Sandage & Fouts (1987). This value of $V_{\rm esc}$ is used to constrain $\Phi_{\rm ELS}$, as described in the Appendix. We note that the inclusion/exclusion of this star hardly affects the following analysis.

The SLZ potential $\Phi(R, z)_{\rm SLZ}$ consists of two components corresponding to a flattened, perfectly oblate disk and a slightly oblate, massive halo. The latter is modeled by the analytic $s = 2$ model of de Zeeuw, Peletier, & Franx (1986), which yields a density profile $\rho(R = 0,\ z) \propto 1/(z^2 + c^2)$ along the z-axis, where c is a constant. This potential provides a nearly flat rotation curve beyond $R = 4$ kpc and reproduces well the local mass density at $R_\odot$. We adopt the values of the parameters in $\Phi(R, z)_{\rm SLZ}$ that were determined by SLZ. We note that the large escape velocity $V_{\rm esc}$ reported above can be attributed to the massive halo. The actual value of $V_{\rm esc}$ is reproduced by setting an arbitrary boundary or tidal radius at the edge of the halo. This method of tuning the potential produces essentially no quantitative change for the orbital properties of stars inside the boundary.

4.2. *Eccentricity versus Metallicity*

Using a model gravitational potential we compute the orbital eccentricity, defined as $e = (r_{\rm ap} - r_{\rm pr})/(r_{\rm ap} + r_{\rm pr})$, where $r_{\rm ap}$ and $r_{\rm pr}$ denote the apogalactic and perigalactic distances, respectively. In Figure 8, we plot our sample stars in the e-[Fe/H] plane, with the eccentricities based on either $\Phi(R)_{\rm ELS}$ (Fig. 8*a*) or $\Phi(R, z)_{\rm SLZ}$ (Fig. 8*b*). Contrary to the ELS result, there is no apparent correlation between e and [Fe/H] for stars with [Fe/H] ≤ -1, as has been claimed by previous workers (Yoshii & Saio 1979; NBP; Carney & Latham 1986; Carney, Latham, & Laird 1990; Norris & Ryan 1991). The orbital motions of stars in this metallicity range are dominated by high-e orbits, but a finite fraction of stars have small-e orbits, even in the [Fe/H] ≤ -1.6 range.

We note that the result for [Fe/H] ≤ -1.6 is almost unchanged by ATT's revised [Fe/H] calibration for metal-poor red giants, because this revised calibration is only effective at [Fe/H] ~ -1.2. Thus we conclude that the orbital motions of metal-poor halo stars in the solar neighborhood are indeed characterized by a diverse distribution of eccentricities. This is more clearly demonstrated by the differential distribution $n(e)$ shown in Figure 9 and the cumulative distribution $N(<e)$ in Figure 10 for the ELS eccentricity (Fig. 10*a*) and the SLZ eccentricity (Fig. 10*b*), where the solid and dotted histograms represent the stars with [Fe/H] ≤ -1.6 and $-1.6 <$ [Fe/H] ≤ -1, respectively. Our sample stars with [Fe/H] ≤ -1.6 and $e < 0.4$ constitute 13% for the ELS eccentricity and 16% for the SLZ eccentricity.

Special attention has been paid to search for metal-poor halo stars with small-e orbits, because their existence constrains the dynamical evolution of the Galaxy (ELS; Yoshii & Saio 1979). NBP claimed that 20% of stars with

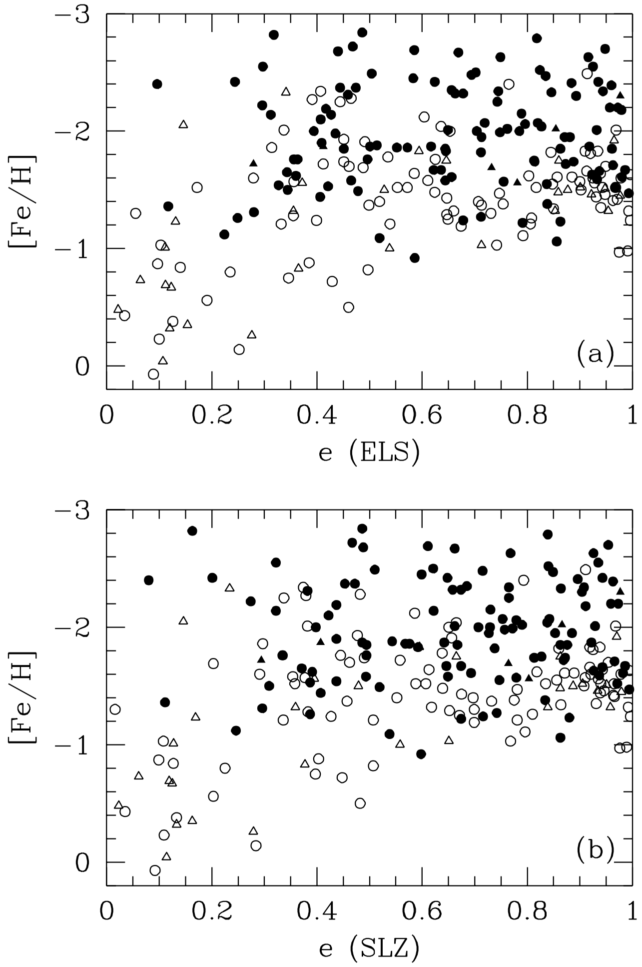

FIG. 8.—Relation between [Fe/H] and e for (*a*) the ELS gravitational potential and (*b*) the SLZ gravitational potential. Symbols are the same as in Fig. 2.

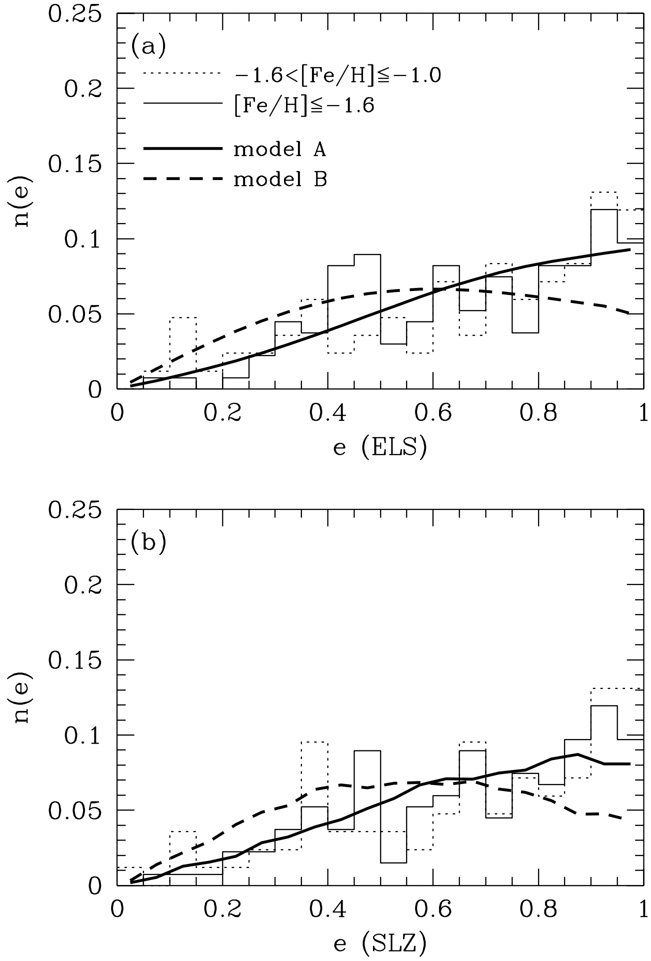

FIG. 9.—Normalized differential e-distribution $n(e)$ for the sample stars with $[\mathrm{Fe/H}] \leq -1.6$ (*solid histograms*) and $-1.6 < [\mathrm{Fe/H}] \leq -1$ (*dotted histograms*). Solid and dashed curves denote the model predictions based on a single Gaussian velocity distribution with a radially anisotropic [$(\sigma_U, \sigma_V, \sigma_W) = (161, 115, 108)$ km s^{-1}] and a tangentially anisotropic [(115, 161, 108) km s^{-1}] velocity ellipsoid, respectively. The former velocity ellipsoid is derived from stars with $[\mathrm{Fe/H}] \leq -1.6$, whereas the latter is just for purposes of comparison.

$[\mathrm{Fe/H}] < -1$ have $e < 0.4$ in their non–kinematically selected sample, whereas Carney & Latham (1986) found 5%–8% in their sample of red giants with $[\mathrm{Fe/H}] < -1.5$. Subsequent workers have further obtained a fraction with $e < 0.4$ ranging from a few percent to a few tens of percent (Carney, Latham, & Laird 1990; Norris & Ryan 1991). In particular, the fraction of such stars has recently been discussed in the context of examining whether the MWTD is a significant component in the Galaxy (Ryan & Lambert 1995; Norris 1996).

It is worth noting that there are several effects that change the estimated fraction of metal-poor stars with low eccentricity. First, a sample selected from high proper motion stars has a significant bias against low eccentricity (Yoshii & Saio 1979; Norris 1986). Second, systematic errors in the [Fe/H] calibration affect the number of stars counted in the respective range of [Fe/H]. Specifically, previous analyses using the [Fe/H] calibration by NBP or MFF for red giants are subject to this effect (Twarog & Anthony-Twarog 1994; Ryan & Lambert 1995). Third, an estimation of e is *not* insensitive to the Galactic gravitational potential. Most prior workers used the original or modified planar ELS potential to obtain the projected e onto the Galactic plane, except for Yoshii & Saio (1979) and Carney et al. (1990), who used a vertically extended gravitational potential. Yoshii & Saio (1979) demonstrated that use of the planar ELS potential overestimates e.

We note that there is a freedom of changing the basic parameters even in the ELS potential. These are the radial scale length and amplitude of the potential, which are scaled by $R_\odot$ and $V_\odot$, respectively. In their original paper, ELS adopted $R_\odot = 10$ kpc and $V_\odot = 250$ km s^{-1}, and these values have also been used by NBP and subsequent workers. Carney et al. (1990) adapted the ELS potential to the updated values of $R_\odot = 8$ kpc and $V_\odot = 220$ km s^{-1}, whereas we use $R_\odot = 8.5$ kpc and $V_\odot = 220$ km s^{-1} together with an extra constraint on V_{esc} (see Appendix). Table 6 summarizes how these changes of the parameters affect the fraction of stars with $[\mathrm{Fe/H}] \leq -1.6$ and $e < 0.4$ in our sample. It can be seen that a potential that yields a greater mass density in the solar neighborhood has the effects of binding the stars more tightly and reducing their apogalactic distances and eccentricities, so that the number of stars with low eccentricity is increased. Accordingly, we emphasize that the reported fraction of metal-poor stars with $e < 0.4$ is inevitably dependent on what form of Galactic gravitational potential is adopted.

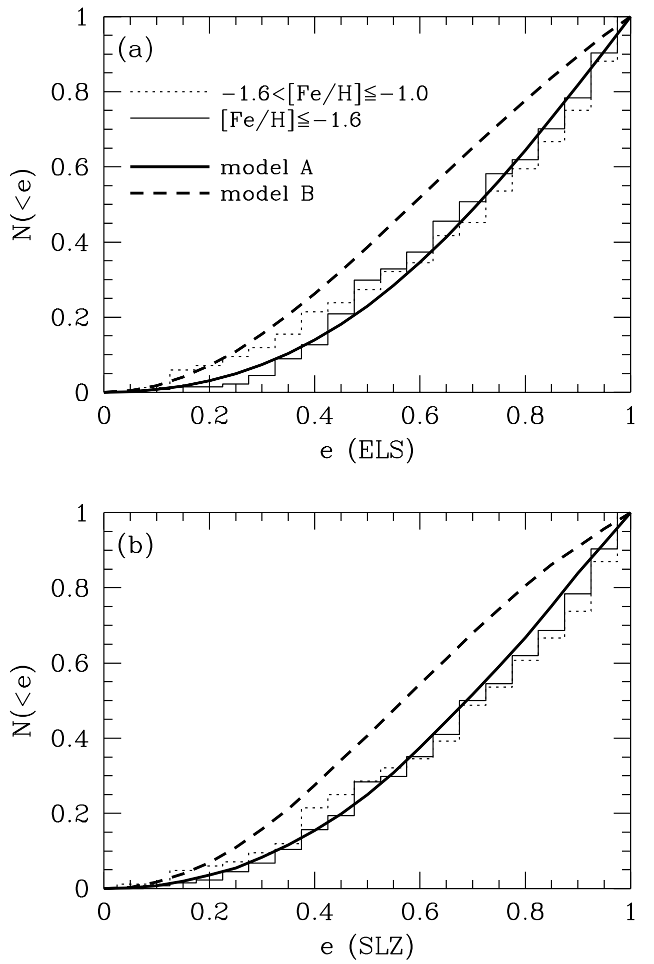

FIG. 10.—Same as Fig. 9, but showing the cumulative e-distribution $N(<e)$ for the sample.

4.3. *Model Eccentricity Distribution for Halo Stars*

Given a fraction of low-metallicity and low-e stars in our sample, we examine whether such fraction is consistent with that expected from the velocity distribution of halo stars.

In § 3, we obtained the velocity distribution for metal-poor stars in the solar neighborhood. This is approximately Gaussian and the velocity ellipsoid is radially elongated,

TABLE 6

FRACTION OF SMALL PLANAR-e ORBITS FOR THE ELS POTENTIAL

	Fraction with $e < 0.4$ (%)	
Case	Observed	Predicted[a]
$R_\odot = 8.5$ kpc, $V_\odot = 220$ km s^{-1}		
$V_{esc} = 450$ km s^{-1}	12.7	13.9
$V_{esc} = 400$ km s^{-1}	10.5	11.4
$V_{esc} = 500$ km s^{-1}	17.9	15.8
No Constraint on V_{esc}		
$R_\odot = 8$ kpc, $V_\odot = 220$ km s^{-1}[b]	5.3	8.7
$R_\odot = 10$ kpc, $V_\odot = 250$ km s^{-1}[c]	4.5	7.6

NOTE.—For [Fe/H] ≤ -1.6.
[a] For $(\sigma_U, \sigma_V) = (161, 115)$ km s^{-1} (see text for details).
[b] Parameters adopted by Carney et al. 1990.
[c] Parameters adopted by ELS and NBP.

with $(\sigma_U, \sigma_V, \sigma_W) = (161, 115, 108)$ km s^{-1} for [Fe/H] < -1.6. The expected distribution of eccentricities is tightly related to this velocity distribution for the elongated orbital motions of stars that arrive near the Sun.

To demonstrate this situation graphically, we show in Figure 11 the so-called Bottlinger diagram in the U-V plane, where curves represent the loci of constant eccentricity derived from Φ_{ELS}. Obviously, stars with eccentricity less than e are enclosed within a locus of constant e in this diagram. For nonzero W-velocities, such stars are enclosed within a surface of constant e in the full (U, V, W)-space. In this way, for a given velocity distribution we obtain the corresponding e-distribution, which depends on the adopted form of the gravitational potential.

We assume that the velocity distribution of halo stars is given by a single Gaussian with no net rotation:

$$f(U, V, W) = \frac{1}{(2\pi)^{3/2}\sigma_U \sigma_V \sigma_W} \times \exp\left[-\frac{U^2}{2\sigma_U^2} - \frac{(V + V_{LSR})^2}{2\sigma_V^2} - \frac{W^2}{2\sigma_W^2}\right], \quad (4)$$

where $V_{LSR} = 220$ km s^{-1}. When the planar potential Φ_{ELS} is used, we can set $W = 0$ in equation (4), and the cumulative e-distribution $N(<e)$ is obtained by integrating $f(U, V, W = 0)$ over the U-V plane within a locus of constant e. For the three-dimensional potential Φ_{SLZ}, we perform a Monte Carlo simulation by creating an ensemble of stars based on $f(U, V, W)$ and estimate e for each star. Here the analytic nature of Φ_{SLZ} has the great advantage of allowing quick estimation of the e-distribution for numerous simulated stars, whereas the procedure is quite time-consuming for a nonanalytic potential, for which numerical integrations of orbits are required.

We consider (1) a radially elongated ellipsoid derived from the stars with [Fe/H] < -1.6 and $(\sigma_U, \sigma_V, \sigma_W) = (161, 115, 108)$ km s^{-1} (model A) and (2) a tangentially elongated

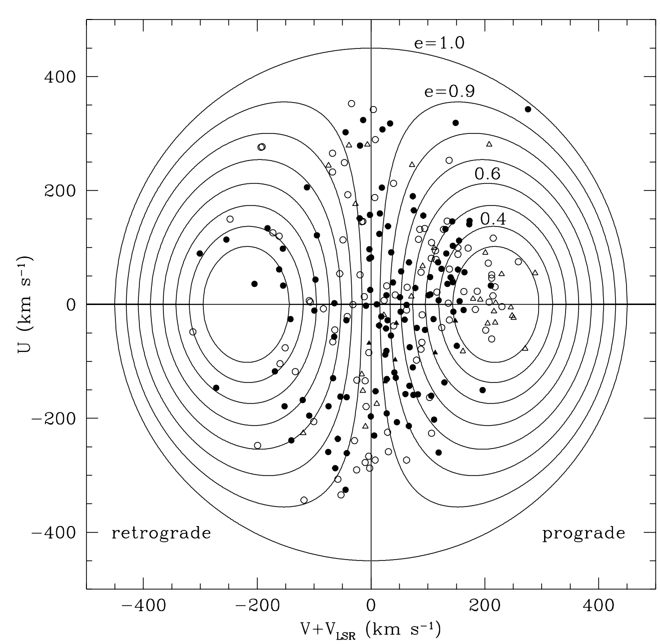

FIG. 11.—Bottlinger diagram for the sample stars. Symbols are the same as in Fig. 2. Each curve denotes a locus of constant e derived from the ELS gravitational potential.

ellipsoid [(115, 161, 108) km s^{-1}], motivated for the purpose of comparison by interchanging σ_U and σ_V. The results for these different velocity ellipsoids are shown by solid and dashed curves, respectively, in Figures 9 and 10.

It is remarkable that such a radially elongated velocity ellipsoid yields an e-distribution that agrees well with the observations for [Fe/H] ≤ -1.6. This is still the case if we use a potential with different values of V_{esc}, $R_\odot$, and $V_\odot$, as shown in Table 6. Some slight differences between the model and the observed e-distributions may have arisen from (1) statistical fluctuation due to the smallness of our sample size, (2) weak dependence of the velocity distribution on the spatial coordinates adopted in the analysis, and (3) slight deviation from a pure Gaussian velocity distribution. Nonetheless, the reasonably good fit of the model curve suggests that the observed e-distribution for [Fe/H] ≤ -1.6 and the fraction of small-e orbits ($e < 0.4$) are naturally explained by a single Gaussian velocity distribution of only the halo component, characterized by a radially elongated velocity ellipsoid. This implies that to explain the existence of such low-metallicity and low-e stars it is *no longer* necessary to introduce an extra MWTD component extending down to [Fe/H] ≤ -1.6. It is interesting to note that if the velocity distribution is tangentially anisotropic, as argued by Sommer-Larsen, Flynn, & Christensen (1994) from their sample stars at large Galactocentric distances, we would observe the e-distribution shown by the dashed curves in Figures 9 and 10.

Our sample stars in Figures 9 and 10 are not restricted to stars with small errors σ_e in derived eccentricity. NBP imposed the criterion $\sigma_e \leq 0.1$, but this has been claimed to produce an extra bias against stars with small proper motions or, perhaps, low eccentricities (Carney & Latham 1986; Twarog & Anthony-Twarog 1994). To see whether this is also the case in our *Hipparcos* sample, we plot σ_e versus e (ELS) in Figure 12. It is evident that only the intermediate-e orbits ($e \sim 0.4$–0.5) suffer from large errors ($\sigma_e > 0.1$). The relatively small errors for small-e orbits may be attributed to the accurate measurements of small proper motions by *Hipparcos* (see Fig. 2). Therefore, the fraction of small-e orbits is unchanged if we confine ourselves to the stars with $\sigma_e \leq 0.1$. This criterion instead eliminates quite a number of stars with $e = 0.4$–0.5 and therefore reduces the observed excess over the predicted e-distribution seen in Figure 9, which further strengthens the conclusion obtained here.

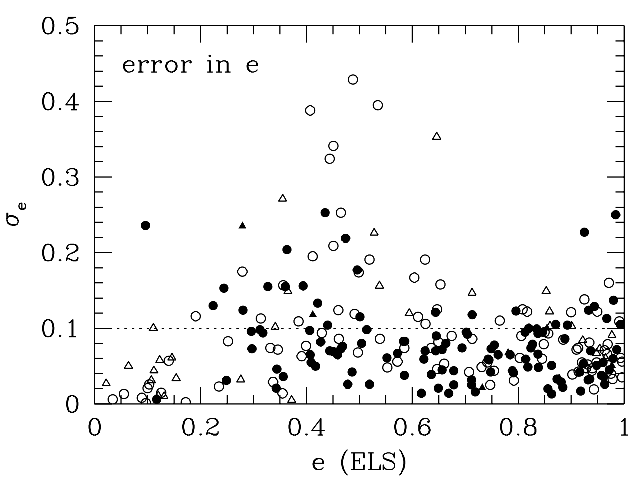

FIG. 12.—Distribution of errors σ_e in e for the ELS gravitational potential.

4.4. *Effects of the Metal-weak Thick Disk on the e-Distribution*

Figure 10 further indicates that the observed fraction of $e < 0.4$ stars in the metallicity range $-1.6 <$ [Fe/H] ≤ -1 appears to be systematically larger than that expected solely from the velocity distribution with [Fe/H] ≤ -1.6. In order to see whether this excess belongs to the MWTD component, we select the stars at $|z| < 1$ kpc as in § 3.2 and derive the cumulative e-distribution $N(<e)$ based on Φ_{SLZ}. The results for $-1.4 <$ [Fe/H] ≤ -1, $-1.6 <$ [Fe/H] ≤ -1, and [Fe/H] ≤ -1.6 are shown by dashed, dotted, and solid histograms, respectively, in Figure 13*a*. Solid curves show the model $N(<e)$ expected from (σ_U, σ_V, σ_W) = (165, 120, 107) km s^{-1} for stars at $|z| < 1$ kpc with [Fe/H] < -1.6. The model again reproduces the observation for [Fe/H] ≤ -1.6 reasonably well.

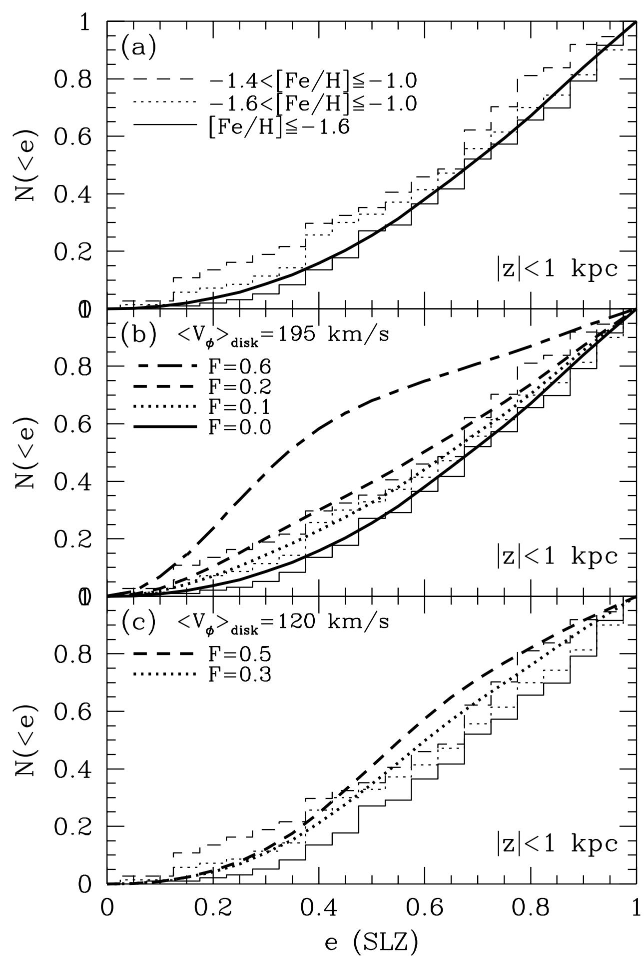

FIG. 13.—Cumulative e-distribution for the stars at $|z| < 1$ kpc, in the metallicity ranges [Fe/H] ≤ -1.6 (*solid histograms*), $-1.6 <$ [Fe/H] ≤ -1 (*dotted histograms*), and $-1.4 <$ [Fe/H] ≤ -1 (*dashed histograms*). The SLZ gravitational potential is used. The solid curve in (*a*) corresponds to the model prediction using the velocity ellipsoid (σ_U, σ_V, σ_W) = (165, 120, 107) km s^{-1} obtained for stars at $|z| < 1$ kpc with [Fe/H] < -1.6. The various curves in (*b*) and (*c*) denote the model results based on a mixture of two Gaussian components (thick disk plus halo). The quantity F denotes the fraction of the thick disk component; (*b*) is for a mean disk rotation $\langle V_\phi \rangle_{disk} = 195$ km s^{-1}, while (*c*) is for $\langle V_\phi \rangle_{disk} = 120$ km s^{-1}.

It is evident that the low-e stars with $[Fe/H] > -1.6$, which may belong to the MWTD, indeed occupy a larger fraction beyond the prediction at lower e. This observed excess is even larger for $-1.4 < [Fe/H] \leq -1$ than for $-1.6 < [Fe/H] \leq -1$. This and the following result remain unchanged even if we use Φ_{ELS} instead of Φ_{SLZ}. Similarly, as in § 3.2, we here attempt to explain this excess component in terms of either (1) the rapidly rotating MWTD at $\langle V_\phi \rangle_{disk} = 195$ km s^{-1} or (2) the slowly rotating MWTD at $\langle V_\phi \rangle_{disk} = 120$ km s^{-1}. The model calculation is performed by using a mixture of two Gaussian velocity distributions that consist of the nonrotating halo and the rotating MWTD at $\langle V_\phi \rangle_{disk}$. For the nonrotating halo we adopt the velocity dispersion for stars at $|z| < 1$ kpc with $[Fe/H] < -1.6$, while the velocity distribution for the MWTD is taken from Beers & Sommer-Larsen's (1995) result $(\sigma_U, \sigma_V, \sigma_W) = (63, 42, 38)$ km s^{-1} for their thick-disk stars at $|z| < 1$ kpc. The MWTD component is assumed to constitute the fraction F.

Figure 13 shows the model $N(<e)$ distributions for $\langle V_\phi \rangle_{disk} = 195$ km s^{-1} (Fig. 13*b*) and $\langle V_\phi \rangle_{disk} = 120$ km s^{-1} (Fig. 13*c*). It follows from Figure 13*b* that the rapidly rotating MWTD at $\langle V_\phi \rangle_{disk} = 195$ km s^{-1} explains the excess for $[Fe/H] > -1.6$ provided that F is as small as a few tenths [$F = 0.2$ for $-1.4 < [Fe/H] \leq -1$ (*dashed curve*) or $F = 0.1$ for $-1.6 < [Fe/H] \leq -1$ (*dotted curve*)].[3] Contrary to the claim by MFF and Beers & Sommer-Larsen (1995), there is no evidence supporting a much higher fraction of this MWTD component (see the model for $F = 0.6$, *short-dash–long-dashed curve*). On the contrary, the slowly rotating MWTD at $\langle V_\phi \rangle_{disk} = 120$ km s^{-1} fails to reproduce the excess at lower e even if F is increased (Fig. 13*c*). It is worth noting that the likelihood analysis in § 3.2 using the V_ϕ-distribution yields larger F for a more slowly rotating MWTD. This does not necessarily indicate that the MWTD component with slower rotation is preferentially confirmed, since the V_ϕ-distribution conveys only partial information on the full three-dimensional orbital motions of stars.

We now turn to the question of how far the MWTD extends above or below the disk plane. In Figure 14*a* we show the cumulative distribution $N(<e)$ for stars at $|z| \geq 1$ kpc. It is of particular interest that the e-distribution for $[Fe/H] \leq -1.6$ (*solid histogram*) remains essentially unchanged when stars are selected at high $|z|$. On the other hand, the fraction of small-e orbits is greatly reduced for both $-1.6 < [Fe/H] \leq -1$ (*dotted histogram*) and $-1.4 < [Fe/H] \leq -1$ (*dashed histogram*). This apparent lack of low-e stars at $|z| \geq 1$ kpc is seen from the [Fe/H] versus e diagram in Figure 14*b*, where the stars with $e < 0.6$ are absent in the metal-poor range $-1.6 < [Fe/H] \leq -1$ and in the metal-rich range $[Fe/H] > -0.8$ (the region enclosed by the dotted line).

More direct insight into the vertical extent of the MWTD is obtained from Figure 15, where the fraction of stars with $e < 0.4$ is shown as a function of the limiting height z_{lim} above or below which the stars are located, i.e., $|z| \geq z_{lim}$. This fraction drops sharply at $z_{lim} = 0.8$–1 kpc for stars with $-1.6 < [Fe/H] \leq -1$ (*dotted curve*) or $-1.4 < [Fe/H] \leq -1$ (*dashed curve*), while it remains almost constant for stars with $[Fe/H] \leq -1.6$ (*solid curve*). Thus the

[3] Even if we adopt a cooler halo velocity ellipsoid as obtained by some previous workers [e.g., $(\sigma_U, \sigma_V, \sigma_W) = (130, 100, 90)$ km s^{-1}], we see a change of only a few percent in the value of F.

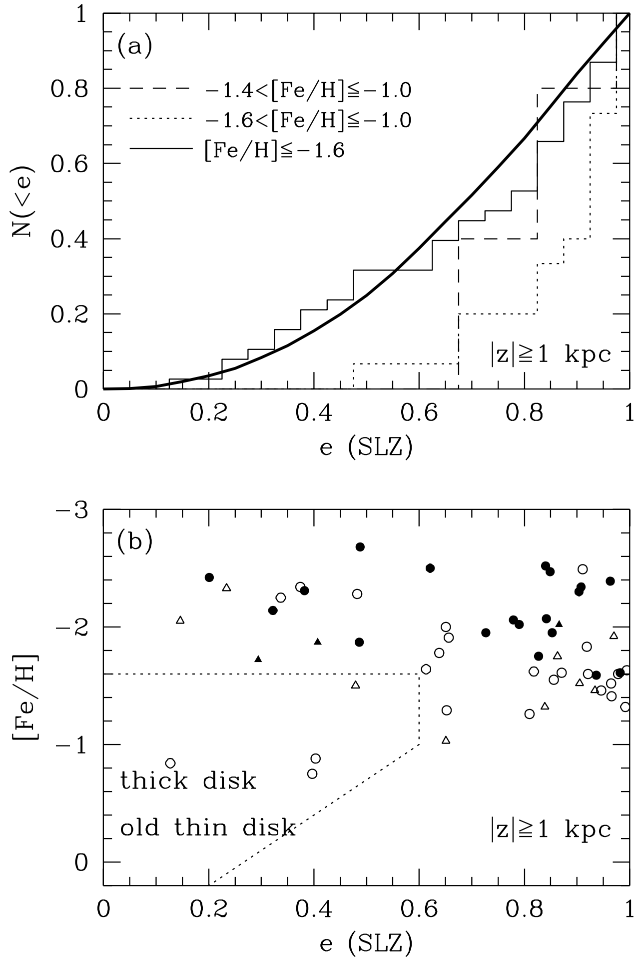

FIG. 14.—(*a*) Normalized cumulative e-distribution for stars at $|z| \geq 1$ kpc. The solid curve is the same as that in Fig. 10 (model A). (*b*) Relation between [Fe/H] and e at $|z| \geq 1$ kpc for the SLZ gravitational potential. Note that, when comparing with Fig. 8 for all z, stars enclosed by the dotted line are selectively excluded by the constraint $|z| \geq 1$ kpc.

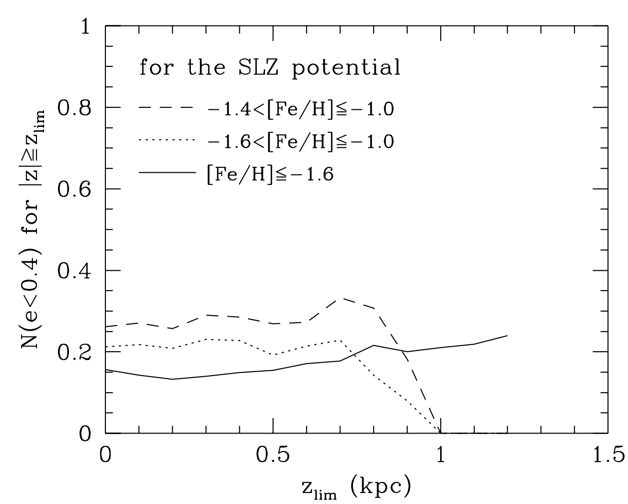

FIG. 15.—Ratio of stars with $e < 0.4$ for $|z| \geq z_{lim}$, as a function of z_{lim}. Solid, dotted, and dashed curves are for $[Fe/H] \leq -1.6$, $-1.6 < [Fe/H] \leq -1$, and $-1.4 < [Fe/H] \leq -1$, respectively. Note the sharp decrease of the curves at $z_{lim} = 0.8$–1 kpc for the intermediate-metallicity range, whereas the curve for $[Fe/H] \leq -1.6$ remains essentially unchanged at large z_{lim}.

rapidly rotating MWTD component, which we have identified in the metal-poor range $-1.6 < [\mathrm{Fe/H}] \leq -1$, has a vertical extent of 0.8–1 kpc. This is virtually consistent with current estimates of the thick disk's scale height (e.g., Yoshii, Ishida, & Stobie 1987). It should also be noted that the halo component, which is exclusively represented by stars with $[\mathrm{Fe/H}] \leq -1.6$, shows no significant dependence on z_{lim} (*solid curve*) and no noticeable contamination from the rapidly rotating MWTD. The low-*e* fraction for $[\mathrm{Fe/H}] \leq -1.6$ slightly increases toward higher z_{lim}. This may be explained by the fact that a star located farther from the solar neighborhood has a smaller radial range in its orbital motion when a set of integrals of motion is given (Yoshii & Saio 1979).

5. METALLICITY GRADIENT AS A CLUE TO FORMATION HISTORY

5.1. *Introduction*

Whether the Galaxy has a global metallicity gradient has been another key issue to understanding its early evolution. ELS used the $|W|$-velocity as an indicator of the maximum vertical height $|z_{\max}|$ that stars can reach, and the ultraviolet excess $\delta(U-B)$ as an indicator of the metallicity corresponding to the epoch at which stars were born from the gas. ELS therefore argued that the correlation between $\delta(U-B)$ and $|W|$ may have arisen if the more metal-poor, older populations were formed at systematically larger heights beyond the disk; in other words, the Galaxy may have collapsed from an extended gas sphere to a disk.

This argument implies that the presence or absence of a large-scale metallicity gradient depends on the balance of competing timescales between the collapse of the Galaxy, the metal enrichment, and the spatial mixing of heavy elements in the gas (see also Sandage & Fouts 1987). In the free-falling proto-Galaxy via dissipation, the gas was progressively confined to smaller volumes, while newly formed stars were left over from this infalling gas. This indicates a higher metallicity for stars that were formed within smaller volumes, thereby causing the metallicity gradient. On the contrary, if the Galaxy was formed in a discontinuous or inhomogeneous manner, e.g., by merging of numerous fragments, such as dwarf-type galaxies, that have their own chemical histories (SZ), no global metallicity gradient would be observed in any spatial direction.

Figure 4 has already shown that a monotonic increase of the $|W|$-velocity with decreasing [Fe/H] is just detectable at $[\mathrm{Fe/H}] > -1.4$ but not apparent at $[\mathrm{Fe/H}] < -1.4$. It is important here to caution that the $|W|$-velocity alone does not characterize $|z_{\max}|$ in a three-dimensional gravitational potential. As we demonstrate graphically in Figure 16, our sample stars observed in the solar neighborhood have traveled through more distant regions of the Galaxy. For instance, a star now at $(R, z) \sim (8.6, -0.5)$ kpc can orbit in the accessible area enclosed by the solid line, whereas a star at $(R, z) \sim (8.6, 0.0)$ kpc is restriced to within the dotted line. Since the orbital z-motion is coupled with those in the R- and ϕ-directions, $|W|$ is not necessarily related to $|z_{\max}|$, especially for stars with a large $|W|$-velocity or large asymmetric drift (see Carney et al. 1990).

We next estimate the maximum height $|z_{\max}|$ and the apogalactic cylindrical distance $R_{\max}$ for each star using SLZ's gravitational potential and then examine how the estimates of $|z_{\max}|$ and $R_{\max}$ for our sample stars are related to their metal abundances. We first divide our sample into four bins of $V_\phi \leq \infty$, 170, 120, and 70 km s^{-1}. The halo component among various populations is extracted simply by selecting stars with small azimuthal velocity V_ϕ (Sandage & Fouts 1987; Carney et al. 1990; see also § 3). However, it is admittedly more problematic to discriminate the MWTD component alone. If we select large-V_ϕ stars assuming that the MWTD is rapidly rotating, the resultant sample will be considerably contaminated by the old disk component of metal-rich stars with $[\mathrm{Fe/H}] > -0.6$. To avoid such a sampling bias, we attempt to discriminate the MWTD component from the small-V_ϕ halo component. We take advantage of the result from § 4 that the MWTD stars likely have smaller e than the halo stars and that their vertical distribution is confined within $|z| < 1$ kpc. Accordingly, we impose the additional constraints $e \leq 0.6$ and $|z| < 1$ kpc to discriminate the MWTD from the halo component.

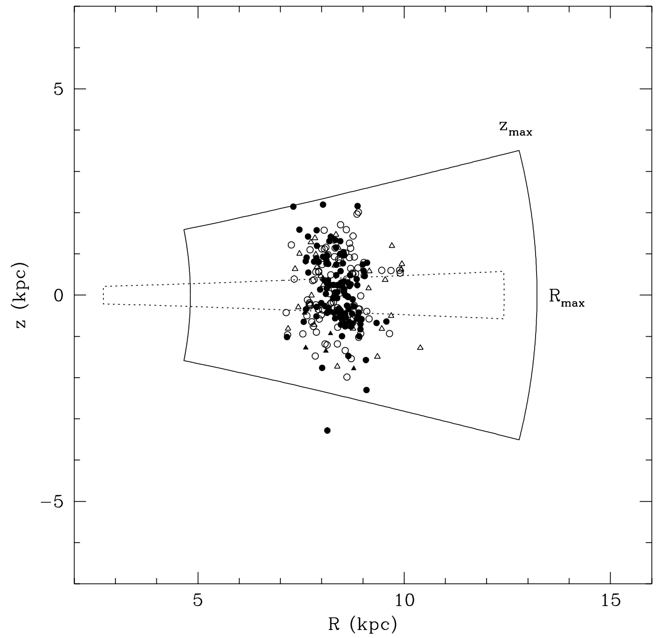

FIG. 16.—Spatial distribution of the sample stars in (R, z). The area enclosed by solid lines corresponds to the domain of orbital motions for HIC 3554 at $(R, z) = (8.58, -0.54)$ kpc, whereas dotted lines are for HIC 2413 at $(R, z) = (8.62, -0.02)$ kpc. The SLZ gravitational model is used.

5.2. *Results*

Plots of [Fe/H] against $R_{\max}$ and similar plots against $|z_{\max}|$ are shown in Figures 17 and 18, respectively, for (*a*) $V_\phi \leq \infty$, or all stars, (*b*) $V_\phi \leq 170$ km s^{-1}, and (*c*) $V_\phi \leq 120$ km s^{-1}. Note that the V_ϕ criteria used in the lower two panels of these figures successfully select halo stars with $[\mathrm{Fe/H}] < -1$. The mean metal abundances in five bins of $R_{\max}$ and in six bins of $|z_{\max}|$ are connected by solid lines with estimated 1 σ errors of the means. These data are listed in Tables 7 and 8, where the results for $V_\phi \leq 70$ km s^{-1} are also tabulated. These figures and tables clearly indicate that stars with $V_\phi \leq 170$ or 120 km s^{-1} show no large-scale metallicity gradient in the R- and z-directions within a 1 σ error level. This agrees with prior works based on different samples of field stars (Saha 1985; Carney et al. 1990) and halo globular clusters (Zinn 1985).

Figures 19 and 20 show the results for the MWTD candidate stars. We find that the additional constraints of $e \leq 0.6$

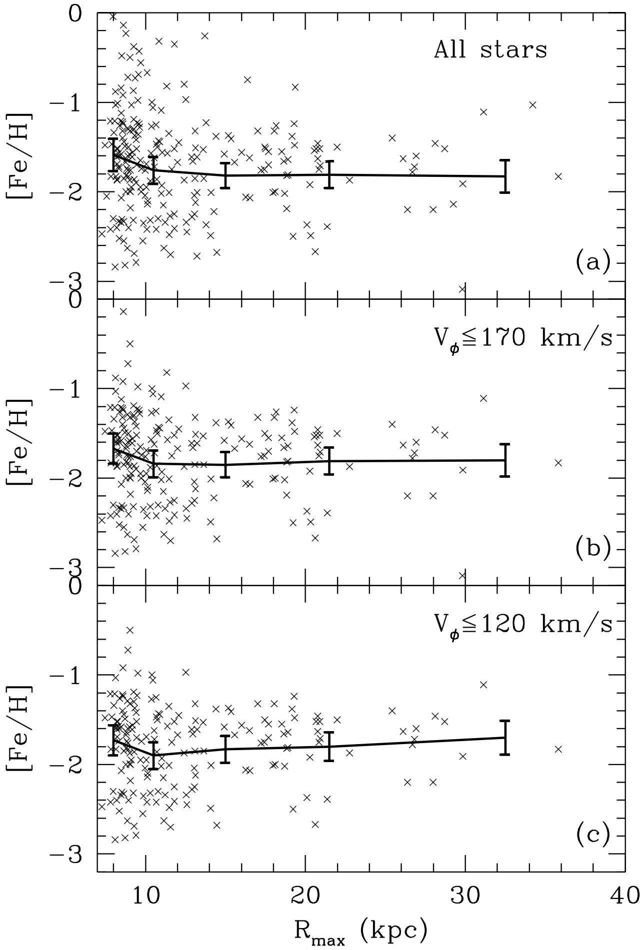

FIG. 17.—Relation between [Fe/H] and R_{max} for the sample (*crosses*) with (*a*) $V_\phi \leq \infty$, (*b*) $V_\phi \leq 170$ km s^{-1}, and (*c*) $V_\phi \leq 120$ km s^{-1}. Error bars denote the mean [Fe/H] and 1 σ errors obtained in different ranges of R_{max}, as tabulated in Table 7, and solid lines trace the mean [Fe/H]. The SLZ gravitational model is used.

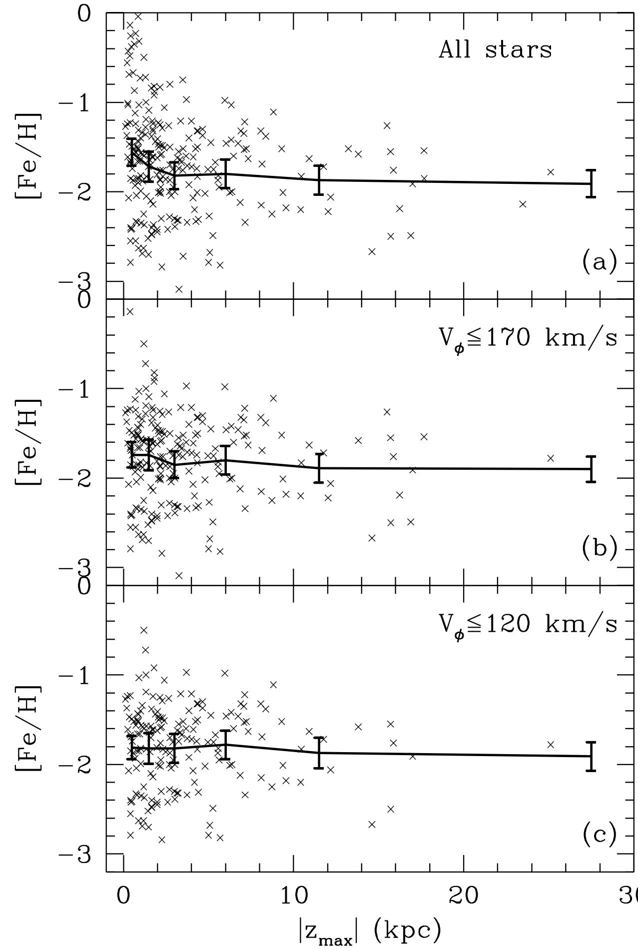

FIG. 18.—Same as Fig. 17, but showing the relation between [Fe/H] and $|z_{max}|$. Error bars denote the mean [Fe/H] and 1 σ errors obtained in different ranges of $|z_{max}|$, as tabulated in Table 8.

and $|z| < 1$ kpc are effective in excluding the very metal-poor stars with [Fe/H] < -1.8. In contrast to the halo component, as discussed above, there is an indication of a metallicity gradient Δ[Fe/H]/$\Delta R_{max} \sim -0.03$ to -0.02 dex kpc^{-1} from $R_{max} = 7$ to $R_{max} = 18$ kpc, and Δ[Fe/H]/$\Delta |z_{max}| \sim -0.07$ to -0.05 dex kpc^{-1} from $|z_{max}| = 1$ to $|z_{max}| = 8$ kpc. The number of MWTD candidates may not be large enough to produce a statistically significant result (see Tables 7 and 8), but it is intriguing to note that the obtained metallicity gradient is larger than the gradient previously detected from the thick-disk stars with [Fe/H] ≥ -1 (see, e.g., Majewski 1993 for a review).

TABLE 7

METALLICITY VERSUS APOGALACTIC CYLINDRICAL DISTANCE

RANGE IN R_{max} (kpc)	$V_\phi \leq \infty$		$V_\phi \leq 170$ km s^{-1}		$V_\phi \leq 120$ km s^{-1}		$V_\phi \leq 70$ km s^{-1}	
	N	⟨[Fe/H]⟩ (dex)	*N*	⟨[Fe/H]⟩ (dex)	*N*	⟨[Fe/H]⟩ (dex)	*N*	⟨[Fe/H]⟩ (dex)
Halo candidates:								
7.0−9.0	50	−1.59 ± 0.18	46	−1.67 ± 0.17	40	−1.73 ± 0.17	31	−1.82 ± 0.15
9.0−12.0	79	−1.76 ± 0.15	73	−1.84 ± 0.15	59	−1.90 ± 0.15	44	−1.95 ± 0.15
12.0−18.0......	37	−1.82 ± 0.14	31	−1.85 ± 0.14	30	−1.83 ± 0.15	24	−1.84 ± 0.14
18.0−25.0......	27	−1.81 ± 0.15	27	−1.81 ± 0.15	23	−1.80 ± 0.16	20	−1.76 ± 0.16
25.0−40.0......	14	−1.83 ± 0.18	13	−1.80 ± 0.18	12	−1.70 ± 0.19	11	−1.69 ± 0.19
MWTD candidates:[a]								
7.0−9.0	22	−1.41 ± 0.20	19	−1.56 ± 0.19	14	−1.62 ± 0.20	7	−1.96 ± 0.14
9.0−12.0	30	−1.47 ± 0.14	24	−1.64 ± 0.14	10	−1.74 ± 0.14	4	−2.13 ± 0.13
12.0−18.0......	12	−1.89 ± 0.15	7	−1.90 ± 0.14	6	−1.84 ± 0.15	3	−1.87 ± 0.10
18.0−25.0......	5	−1.97 ± 0.11	5	−1.97 ± 0.11	1	−2.37 ± 0.05	1	−2.37 ± 0.05
25.0−40.0......	1	−1.72 ± 0.28	1	−1.72 ± 0.28	1	−1.72 ± 0.28	1	−1.72 ± 0.28

[a] With the extra constraints $e \leq 0.6$ and $|z| < 1$ kpc.

TABLE 8

METALLICITY VERSUS MAXIMUM VERTICAL DISTANCE

RANGE IN $\|z_{max}\|$ (kpc)	$V_\phi \le \infty$		$V_\phi \le 170$ km s^{-1}		$V_\phi \le 120$ km s^{-1}		$V_\phi \le 70$ km s^{-1}	
	N	⟨[Fe/H]⟩ (dex)	*N*	⟨[Fe/H]⟩ (dex)	*N*	⟨[Fe/H]⟩ (dex)	*N*	⟨[Fe/H]⟩ (dex)
Halo candidates:								
0.0–1.0	48	-1.56 ± 0.15	41	-1.74 ± 0.14	33	-1.81 ± 0.13	26	-1.84 ± 0.14
1.0–2.0	48	-1.72 ± 0.17	44	-1.74 ± 0.17	38	-1.82 ± 0.17	27	-1.92 ± 0.14
2.0–4.0	48	-1.82 ± 0.15	45	-1.85 ± 0.15	39	-1.82 ± 0.16	32	-1.86 ± 0.16
4.0–8.0	36	-1.80 ± 0.16	35	-1.80 ± 0.16	34	-1.78 ± 0.16	29	-1.77 ± 0.16
8.0–15.0	17	-1.87 ± 0.16	16	-1.89 ± 0.16	15	-1.87 ± 0.17	13	-1.83 ± 0.17
15.0–40.0......	12	-1.91 ± 0.15	10	-1.90 ± 0.14	6	-1.91 ± 0.16	4	-1.99 ± 0.15
MWTD candidates:[a]								
0.0–1.0	20	-1.17 ± 0.17	13	-1.54 ± 0.15	5	-1.71 ± 0.14	3	-1.73 ± 0.17
1.0–2.0	20	-1.53 ± 0.19	17	-1.51 ± 0.20	12	-1.61 ± 0.21	5	-2.18 ± 0.14
2.0–4.0	13	-1.80 ± 0.14	11	-1.81 ± 0.13	6	-1.83 ± 0.14	3	-2.07 ± 0.08
4.0–8.0	7	-1.99 ± 0.14	6	-1.99 ± 0.13	5	-1.93 ± 0.13	3	-2.06 ± 0.10
8.0–15.0	5	-1.75 ± 0.17	4	-1.80 ± 0.18	3	-1.66 ± 0.21	2	-1.71 ± 0.22
15.0–40.0......	5	-1.85 ± 0.14	5	-1.85 ± 0.14	1	-1.76 ± 0.20	0	...

[a] With the extra constraints $e \le 0.6$ and $|z| < 1$ kpc.

Further studies based on the assembly of more sample stars will be important to elucidate this discrepancy and clarify the formation process of this controversial component.

6. DISCUSSION AND CONCLUSION

We have investigated the kinematics of 122 red giant and 124 RR Lyrae stars, which were selected without kinematic bias and were observed by the *Hipparcos* satellite to measure accurately their proper motions. The metal abundances of our program stars range from [Fe/H] $= -1$ to [Fe/H] $= -3$, making them suitable for analyzing the halo component, as well as the metal-weak tail of the thick disk component below [Fe/H] $= -1$. We summarize our results below and discuss them in the context of the early evolution of the Galaxy.

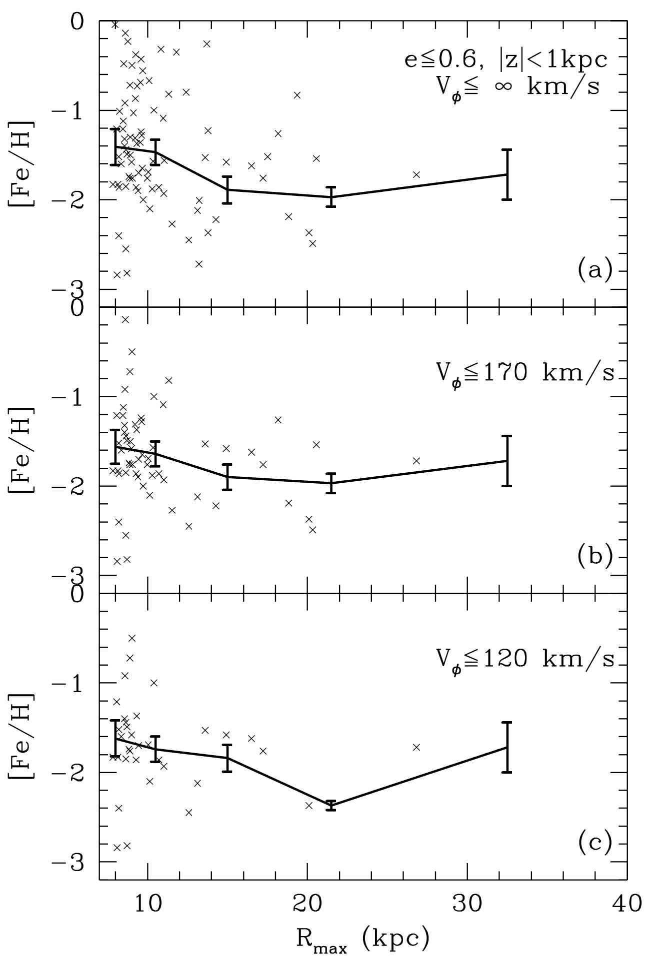

FIG. 19.—Same as Fig. 17, but for the MWTD candidate stars selected with the additional constraints $e \le 0.6$ and $|z| < 1$ kpc.

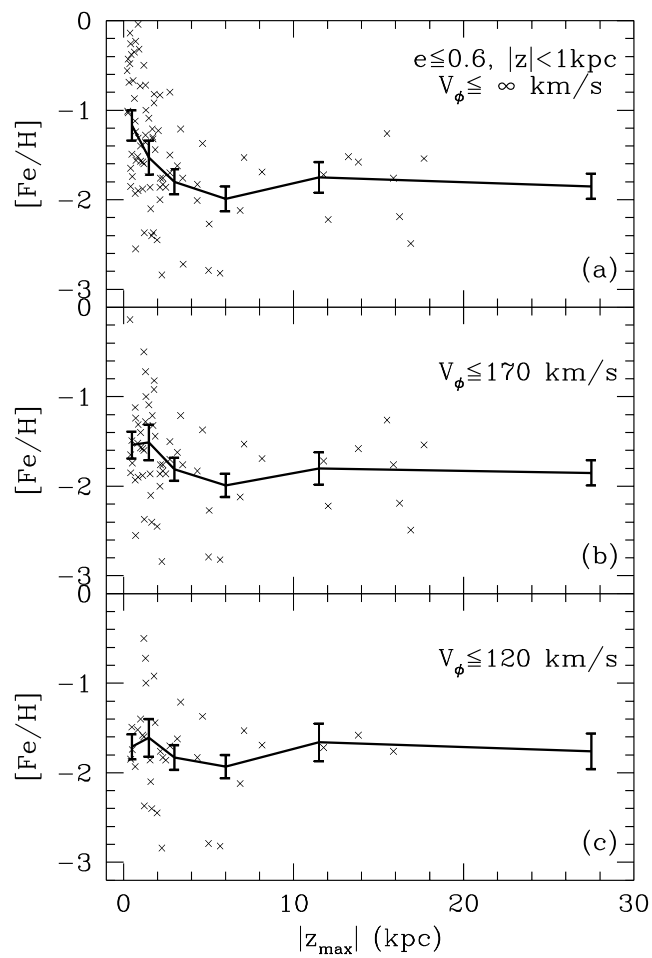

FIG. 20.—Same as Fig. 19, but for [Fe/H] vs. $|z_{max}|$

6.1. *Summary*

The present analyses indicate that the solar neighborhood stars with [Fe/H] ≤ -1 mostly have the halo-like kinematics of large velocity dispersion and no significant rotation. The velocity ellipsoid is radially elongated, with $(\sigma_U, \sigma_V, \sigma_W) = (161, 115, 108)$ km s^{-1} in the metal-poor range [Fe/H] ≤ -1.6. The rotational properties of the system as probed by $\langle V_\phi \rangle$ or $\langle V_\phi \rangle / \sigma_\phi$ appear to change largely at [Fe/H] ~ -1.4 to -1 (Fig. 5), indicating that the collapse of the Galaxy from the halo to the disk took place discontinuously.

We have found no correlation between [Fe/H] and e for [Fe/H] ≤ -1 (Fig. 8), which is in contrast to the result of ELS. Even for [Fe/H] ≤ -1.6, about 16% of our program stars are found to have $e < 0.4$ (the value of e depends slightly on the gravitational potential adopted), and this fraction of low-e stars stems from the radially elongated velocity ellipsoid of the halo component alone, without introducing an extra disk component (Figs. 9 and 10). Thus, the existence of low-e stars does not necessarily imply the dominance of an extra, rapidly rotating component in the metal-poor range ([Fe/H] ≤ -1.6). The conclusion that almost all stars with [Fe/H] ≤ -1.6 belong to the halo component is supported by the absence of a significant change in the e-distribution with increasing $|z|$ (Figs. 14*a* and 15). We have also found no large-scale metallicity gradient in the halo in either the radial or the vertical direction (Figs. 17 and 18).

Many workers have claimed the existence of a metal-weak tail of the thick disk component in the range $-1.6 <$ [Fe/H] ≤ -1 (MFF; Beers & Sommer-Larsen 1995). The fraction F of this component is, however, found to be smaller than previously thought. The maximum likelihood technique to fit to the observed V_ϕ-distribution yields $F \sim 0.1$ for $-1.6 <$ [Fe/H] ≤ -1 and $F \sim 0.2$ for $-1.4 <$ [Fe/H] ≤ -1, while $F \sim 0$ for [Fe/H] ≤ -1.6. We have shown that the distribution of orbital eccentricity provides a powerful method for constraining the fraction $F \approx 0.1$–0.2, the mean velocity $\langle V_\phi \rangle_{\rm disk} \approx 195$ km s^{-1}, and the vertical extent $z_{\rm lim} \approx 0.8$–1 kpc of this extra disk component (Figs. 13–15). We emphasize that this new approach is effective only if accurate proper motions are available, such as from an astrometric satellite like *Hipparcos*.

We conclude from our results that the extra metal-weak disk that we have identified is the metal-weak tail of the rapidly rotating thick disk that dominates in the range [Fe/H] $= -0.6$ to -1. This is therefore consistent with the claim by MFF and Beers & Sommer-Larsen (1995), although our estimate of $F \approx 0.1$–0.2 is much smaller than theirs. Using a full knowledge of the orbital motions of these disklike stars, we have obtained a possible indication of the large-scale metallicity gradient in the metal-weak tail of the thick disk component (Figs. 19 and 20).

6.2. *Implications for the Picture of Galaxy Formation*

6.2.1. *Halo Component*

Our finding of no significant [Fe/H]-e relation in the [Fe/H] ≤ -1.6 range conflicts with the ELS scenario that the proto-Galaxy underwent free-fall collapse and that the stars formed out of the falling gas should have eccentric orbits. The presence of low-e halo stars in our sample, although constituting only a small fraction, is a key to understanding how the halo was formed, because such low-e stars belong to the halo but not to the rapidly rotating thick disk.

Our program stars were sampled in the vicinity of the Sun, and only about 16% of the sample have eccentricities below $e = 0.4$. As a direct consequence of the radially elongated velocity ellipsoid, the e-distribution is largely skewed toward higher e. On the other hand, the orbital motions of halo stars sampled at much larger Galactocentric distances remain yet undetermined because of the lack of accurate measurements of their proper motions. However, an intriguing result on the velocity distribution in the outer halo has been derived by Sommer-Larsen et al. (1994), using the radial velocities for their sample of blue horizontal branch stars at $r = 5$–55 kpc. Their analysis indicates that the velocity ellipsoid turns out to be tangentially anisotropic beyond $r \sim 15$ kpc. This implies that high angular momentum, small-e orbits are dominant in the outer halo (Figs. 9 and 10, *dashed curves*). Thus, any scenario for the formation of the Galaxy must explain not only the e-distribution in the solar neighborhood but also the velocity ellipsoid with radial anisotropy transforming into tangential anisotropy with increasing Galactocentric distance.

If one adopts the currently favored scenario that the halo was assembled from merging or accretion of numerous fragments (SZ), no correlation between kinematic and chemical properties is expected, because each fragment, presumably a gas-rich or gas-poor dwarf-type galaxy, has its own chemical history. The SZ scenario is thus successful in explaining the absence of both an [Fe/H]-e relation and a global metallicity gradient derived from the halo stars observed near the Sun. It is also consistent with a wide age spread in globular clusters, as well as in field stars, because star formation in each fragment proceeds independently.

We go on to ask whether the SZ scenario is furthermore consistent with the e-distribution in the solar neighborhood and the change of the velocity ellipsoid with increasing Galactocentric distance. A process of merging or accretion of dwarf-type galaxies involves dynamical friction, which reduces the orbital radius (see, e.g., Quinn, Hernquist, & Fullagar 1993). At some radius below which the mean density of the fragment is exceeded by the mean density of the Galaxy, the fragment is tidally disrupted and the debris is dispersed to constitute the stellar halo. Since dynamical friction tends to circularize the orbit of the fragment, the orbits of remnant stars are weighted in favor of small e. This indicates that the velocity ellipsoid becomes more tangentially anisotropic at smaller Galactocentric distance, which is opposite to the observed trend. Although detailed numerical simulations modeling a number of accretion events are to be explored, the above simple argument implies that the SZ scenario seems unlikely to reproduce the kinematic properties of halo stars.

An alternative scenario of the formation of the Galaxy has been proposed by Sommer-Larsen & Christensen (1989) to explain the change of the velocity ellipsoid with Galactocentric distance. When the proto-Galactic overdense region started to collapse out of cosmological expansion, large fluctuations, developed within the mixture of gas and dark matter, heated the gas up to the virial temperature of $\sim 10^6$ K (which is typical of the Galaxy). This virialized system is largely pressure supported inside the virial radius. Ensembles of gas clouds are isotropically moving at each radius, and dissipative cloud-cloud collisions then induce the formation of halo stars. The collisional rate is orbit dependent.

For example, clouds having more radially eccentric orbits encounter more clouds in denser, inner parts of the Galaxy, so such clouds may never return to the radius from which the orbital motions started. Thus this mechanism favors the survival of systematically more circular orbits at larger radii, which agrees with the kinematic properties of halo stars.

This scenario has been further investigated by Theis (1997), who performed numerical simulations of a collapsing dissipative cloud system. He has successfully obtained tangentially elongated velocity ellipsoids for surviving clouds after the dissipative collapse. It is, however, yet unexplored whether stars formed by this mechanism have the same kinematic and chemical properties as observed. Specifically, since the mechanism involves gaseous dissipation over several free-fall timescales, a large-scale metallicity gradient may appear in the stellar system. In this respect, the effects of energy feedback from massive stellar winds and supernova explosions to the surrounding gas may play an important role in suppressing rapid gaseous dissipation and smearing out any metallicity gradient by rapid mixing of heavy elements in the gas.

A more realistic picture is midway between the above scenarios. The currently favored cold dark matter scenario of galaxy formation indicates that the initial density fluctuations in the early universe have larger amplitudes on smaller scales (see, e.g., Padmanabhan 1993). Hence, the initial overdense regions that end up with giant galaxies like our own contain larger density fluctuations on subgalactic scales. In a collapsing protogalaxy, these small-scale fluctuations develop into numerous fragments that interact together via gravitational force (Katz & Gunn 1991). As a result of torque among fragments or direct merging, angular momentum is transferred from inner to outer regions of the system. Since star formation and chemical evolution progress differently in each fragment, one might expect a wide age spread and no metallicity gradient in the final stellar system. This is indeed indistinguishable from the SZ scenario. If halo stars are formed via inelastic, anisotropic collisional processes between fragments, the kinematics of such stars may well accord with the observed transition of the velocity ellipsoid from the solar neighborhood to the outer halo (Sommer-Larsen & Christensen 1989).

Some of the small density contrasts that have gained systematically higher angular momentum in the course of cosmological expansion may have slowly fallen into the system after most parts of the system were settled. These delayed accretions may explain the reported indications of relatively young stars (Rodgers, Harding, & Sadler 1981) and retrograde-orbit stars (Majewski 1992) in the outer halo, which have been regarded as direct evidence of accretion. It is indeed of great importance to investigate this scenario in more detail, by exploring high-resolution simulations of a collapsing galaxy combined with star formation and chemical evolution, in order to fully understand the kinematic and chemical properties of the halo reported in the present work.

6.2.2. *Thick Disk Component*

How a disk with a large vertical scale height was formed is also enigmatic (see, e.g., Majewski 1993). One leading scenario is that the disk was heated by the merging of satellites with the preexisting thin disk (Quinn et al. 1993). Satellite orbits decayed and were circularized into the disk plane, and then fell toward the center of the disk. The disk stars were spread out by the merging, and the aftermath was reported to be similar to the observed spatial structure and kinematic properties of the thick disk component. According to this scenario, the thin disk was formed after a major merger event. Therefore, timing of this merger event is severely constrained by the presence of the presently observed thin disk, with a vertical scale height of 350 pc. An alternative scenario is that the thick disk may have formed in a dissipative manner after the major parts of the halo formation were completed (see, e.g., Larson 1976; Burkert, Truran, & Hensler 1992; Burkert & Yoshii 1996). Contraction of the disk either occurred in a pressure-supported manner because of the energy feedback or rapidly progressed into the thin disk because of the efficient line cooling.

One of the possible observational clues to discriminate these scenarios lies in the fraction of the thick disk in the metal-poor range ($[Fe/H] \leq -1.6$). In the merger scenario, since the mechanism relies on both the preexisting old disk and merging satellites having different chemical histories, the aftermath of the merger may contain numerous metal-poor stars. On the contrary, in the dissipative collapse scenario, since the gas that forms the thick disk is already enriched by metal ejection of halo stars, few metal-poor stars should be observed in the thick disk. Our finding of essentially no thick-disk stars in the range $[Fe/H] \leq -1.6$ appears to support the latter scenario.

Another clue to clarifying the formation of the thick disk is to examine whether a large-scale metallicity gradient exists. The merger scenario may envisage no metallicity gradient, whereas the dissipative contraction of the disk may involve the smooth spatial variation of metallicity in stars. No consensus has ever been reached on the observational evidence regarding a metallicity gradient in the thick disk (Majewski 1993). However, if our finding of a nonnegligible metallicity gradient in the metal-weak disk is the case, it is possible to deduce that the contraction of the halo into the thick disk occurred in a dissipative manner just after the major parts of the halo formation were completed.

Before concluding definitely, it is necessary to assemble data on more stars with accurate distances and proper motions. The method that we have developed here based on the eccentricity distribution of orbits may be useful for examining whether the thick disk has a significant metal-weak tail, as well as a global metallicity gradient. More elaborate modeling is needed to further clarify the physical connection between the halo and the thick disk and to propose what observations will be the most definite discriminator of the scenarios for the formation of the Galaxy.

We are grateful to H. Saio, T. Tsujimoto, and M. Miyamoto for useful discussions. This work has been supported in part by Grants-in-Aid for Scientific Research (08640318, 09640328) and COE Research (07CE2002) of the Ministry of Education, Science, and Culture in Japan.

APPENDIX

ELS MODEL FOR THE GRAVITATIONAL POTENTIAL

The ELS potential as a function of Galactocentric distance R in the plane is given by

$$\Phi_{\rm ELS}(R) = -\frac{GM}{b + (R^2 + b^2)^{1/2}} , \tag{A1}$$

where M is the total mass of the disk and b is the scale length. For a disk in centrifugal equilibrium, the circular velocity V_c is given by $V_c(R) = (R\, d\Phi_{\rm ELS}/dR)^{1/2}$.

The values of b and M can be evaluated from the Oort constants (A, B) and the circular velocity $V_\odot$ at $R_\odot$, i.e.,

$$-\frac{A + B}{A - B} = \frac{1 + 2q - q^2}{2q^2} , \tag{A2}$$

$$V_c(R_\odot) = V_\odot , \tag{A3}$$

where $q \equiv [(R_\odot/b)^2 + 1]^{1/2}$. For $A = 15$ km s^{-1} kpc^{-1} and $B = -10$ km s^{-1} kpc^{-1}, equation (A2) yields $q = 3.77$, and thus $b = R_\odot/3.65$ kpc. Equation (A3) then reads $(GM/b)^{1/2} = 2.54V_\odot$. ELS adopted $R_\odot = 10$ kpc and $V_\odot = 250$ km s^{-1}, and thereby $b = 2.74$ kpc and $(GM/b)^{1/2} = 635$ km s^{-1}. If $R_\odot = 8$ kpc and $V_\odot = 220$ km s^{-1}, as adopted by Carney et al. (1990), we obtain $b = 2.19$ kpc and $(GM/b)^{1/2} = 559$ km s^{-1}.

In the present work, we use the escape velocity $V_{\rm esc}$ near the Sun as an alternative constraint. The definition $V_{\rm esc} = [2\,|\,\Phi_{\rm ELS}(R_\odot)\,|\,]^{1/2}$ then reads

$$1 - (\sqrt{2}V_\odot/V_{\rm esc})^2 = 1/q , \tag{A4}$$

instead of equation (A2). For $V_\odot = 220$ km s^{-1} and $V_{\rm esc} = 450$ km s^{-1}, we obtain $q = 1.92$, and thus $b = R_\odot/1.63 = 5.2$ kpc. Equation (A3) then reads $(GM/b)^{1/2} = 2.48V_\odot = 545$ km s^{-1} for $V_\odot = 220$ km s^{-1}. This model is characterized by a larger b than previously, to accord with the large $V_{\rm esc}$ observed near the Sun.

REFERENCES

Anthony-Twarog, B. J., & Twarog, B. A. 1994, AJ, 107, 1577 (ATT)
Bahcall, J. N., Schmidt, M., & Soneira, R. M. 1982, ApJ, 258, L23
Barbier-Brossat, M. 1989, A&AS, 80, 67
Beers, T. C., & Sommer-Larsen, J. 1995, ApJS, 96, 175
Blanco, V. M. 1992, AJ, 104, 734
Bond, H. E. 1980, ApJS, 44, 517
Burkert, A., Truran, J. W., & Hensler, G. 1992, ApJ, 391, 651
Burkert, A., & Yoshii, Y. 1996, MNRAS, 282, 1349
Burstein, D., & Heiles, C. 1982, AJ, 87, 1165
Carney, B. W. 1988, in IAU Symp. 126, The Harlow Shapley Symposium on Globular Cluster Systems in Galaxies, ed. J. E. Grindlay & A. G. D. Philip (Dordrecht: Kluwer), 133
Carney, B. W., Aguilar, L., Latham, D. W., & Laird, J. B. 1990, AJ, 99, 201
Carney, B. W., & Latham, D. W. 1986, AJ, 92, 60
Carney, B. W., Latham, D. W., & Laird, J. B. 1990, AJ, 99, 572
Carney, B. W., Storm, J., & Jones, R. V. 1992, ApJ, 386, 663
Clube, S. V. M., & Dawe, J. A. 1980, MNRAS, 190, 591
de Zeeuw, T., Peletier, R., & Franx, M. 1986, MNRAS, 221, 1001
Eggen, O. J., Lynden-Bell, D., & Sandage, A. R. 1962, ApJ, 136, 748 (ELS)
ESA. 1992, The Hipparcos Input Catalogue (ESA SP-1136) (Noordwijk: ESA)
———. 1997, The Hipparcos and Tycho Catalogues (ESA SP-1200) (Noordwijk: ESA)
Evans, D. S. 1978, Bull. Inf. CDS, 15, 121
FitzGerald, M. P. 1968, AJ, 73, 983
———. 1987, MNRAS, 229, 227
Freeman, K. C. 1987, ARA&A, 25, 603
Gilmore, G., & Reid, I. N. 1983, MNRAS, 202, 1025
Griffin, R., Griffin, R., Gustafsson, B., & Vieira, T. 1982, MNRAS, 198, 637
Johnson, D. R. H., & Soderblom, D. R. 1987, AJ, 93, 864
Katz, N., & Gunn, J. E. 1991, ApJ, 377, 365
Klemola, A. R., Hanson, R. B., & Jones, B. F. 1993, Lick Northern Proper Motion Program: NPM1 Catalog (NSSDC/ADC Cat. A1199) (Greenbelt, MD: GSFC)
Kukarkin, B. V., et al. 1969–1976, General Catalogue of Variable Stars (3d ed., 3 vols. and 3 suppls.; Moscow: Nauka)
Laird, J. B., Rupen, M. P., Carney, B. W., & Latham, D. W. 1988, AJ, 96, 1908
Lanzetta, K. M., Wolfe, A. M., & Turnshek, D. A. 1995, ApJ, 440, 435
Larson, R. B. 1976, MNRAS, 170, 31
Layden, A. C. 1994, AJ, 108, 1016
———. 1995, AJ, 110, 2288
Layden, A. C., Hanson, R. B., Hawley, S. L., Klemola, A. R., & Hanley, C. J. 1996, AJ, 112, 2110
Lu, L., Sargent, W. L. W., Barlow, T. A., Churchill, C. W., & Vogt, S. S. 1996, ApJS, 107, 475
Majewski, S. R. 1992, ApJS, 78, 87
———. 1993, ARA&A, 31, 575
Mihalas, D., & Binney, J. 1981, Galactic Astronomy (2d ed.; San Francisco: Freeman)
Morrison, H. L., Flynn, C., & Freeman, K. C. 1990, AJ, 100, 1191 (MFF)
Norris, J. E. 1986, ApJS, 61, 667
———. 1996, in ASP Conf. Ser. 92, Formation of the Galactic Halo—Inside and Out, ed. H. L. Morrison & A. Sarajedini (San Francisco: ASP), 14
Norris, J. E., Bessell, M. S., & Pickles, A. J. 1985, ApJS, 58, 463 (NBP)
Norris, J. E., & Ryan, S. G. 1989, ApJ, 349, 739
———. 1991, ApJ, 380, 403
Padmanabhan, T. 1993, Structure Formation in the Universe (Cambridge: Cambridge Univ. Press)
Perryman, M. A. C., et al. 1995, A&A, 304, 69
Pettini, M., King, D. L., Smith, L. J., & Hunstead, R. W. 1995, in QSO Absorption Lines, ed. G. Meylan (Berlin: Springer), 71
Quinn, P. J., Hernquist, L., & Fullagar, D. P. 1993, ApJ, 403, 74
Rodgers, A. W., Harding, P., & Sadler, E. 1981, ApJ, 244, 912
Rodgers, A. W., & Roberts, W. H. 1993, AJ, 106, 1839
Ryan, S. G., & Lambert, D. L. 1995, AJ, 109, 2068
Ryan, S. G., & Norris, J. E. 1991, AJ, 101, 1865
Saha, A. 1985, ApJ, 289, 310
Sandage, A. R. 1993, AJ, 106, 703
Sandage, A. R., & Fouts, G. 1987, AJ, 93, 74
Schuster, W. J., & Nissen, P. E. 1989, A&A, 222, 69
Searle, L., & Zinn, R. 1978, ApJ, 225, 357 (SZ)
Sommer-Larsen, J., & Christensen, P. R. 1989, MNRAS, 239, 441
Sommer-Larsen, J., Flynn, C., & Christensen, P. R. 1994, MNRAS, 271, 94
Sommer-Larsen, J., & Zhen, C. 1990, MNRAS, 242, 10 (SLZ)
Theis, C. 1997, in ASP Conf. Ser. 112, The History of the Milky Way and Its Satellite System, ed. A. Burkert, D. H. Hartmann, & S. A. Majewski (San Francisco: ASP), 35
Twarog, B. A. & Anthony-Twarog, B. J. 1994, AJ, 107, 1371
———. 1996, AJ, 111, 220
Vogt, N. P., Forbes, D. A., Phillips, A. C., Gronwall, C., Faber, S. M., Illingworth, G. D., & Koo, D. C. 1996, ApJ, 465, L15
Wan, L., Mao, Y.-Q., & Ji, D.-S. 1980, Ann. Shanghai Obs., 2, 1
Wilhelm, R. 1995, Ph.D. thesis, Michigan State Univ.
Williams, R. E., et al. 1996, AJ, 112, 1335
Wilson, R. E. 1953, General Catalogue of Stellar Radial Velocities (Washington: Carnegie Inst. Washington)
Yoshii, Y. 1982, PASJ, 34, 365
Yoshii, Y., Ishida, K., & Stobie, R. S. 1987, AJ, 93, 323
Yoshii, Y., & Saio, H. 1979, PASJ, 31, 339
Zinn, R. 1985, ApJ, 293, 424
———. 1988, in IAU Symp. 126, The Harlow Shapley Symposium on Globular Cluster Systems in Galaxies, ed. J. E. Grindlay & A. G. D. Philip (Dordrecht: Kluwer), 37
Zinn, R., & West, M. J. 1984, ApJS, 55, 45